FACILITY FORM 602

N65-24387
(ACCESSION NUMBER) (THRU)

(PAGES) (CODE)

CR-54369
(NASA CR OR TMX OR AD NUMBER) (CATEGORY)

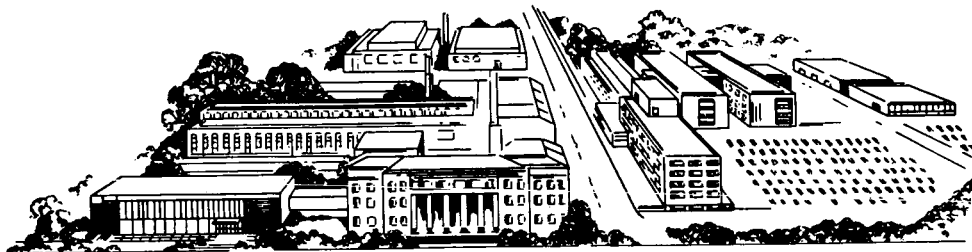# DEVELOPMENT OF A VAPOR-PRESSURE-OPERATED HIGH-TEMPERATURE SENSOR DEVICE

by

J. R. Van Orsdel, G. E. Raines, and J. M. Allen

prepared for

NATIONAL AERONAUTICS AND SPACE ADMINISTRATION

CONTRACT NAS3-5202

BATTELLE
MEMORIAL INSTITUTE

Requests for copies of this report
should be referred to:

National Aeronautics and Space Administration
Office of Scientific and Technical Information
Washington 25, D.C.
Attention: AFSS-A

CASE FILE COPY

FINAL REPORT

on

DEVELOPMENT OF A VAPOR-PRESSURE-OPERATED HIGH-TEMPERATURE SENSOR DEVICE

by

J. R. Van Orsdel, G. E. Raines, and J. M. Allen

prepared for

National Aeronautics and Space Administration

March 11, 1965

Technical Management
NASA-Lewis Research Center
Cleveland, Ohio
Advanced Development and Evaluation Division
Miles O. Dustin

BATTELLE MEMORIAL INSTITUTE
505 King Avenue
Columbus, Ohio 43201

ABSTRACT

2·4387

Vapor-pressure curves for several low melting point metals are presented as a basis for selection of a temperature sensor charging metal.

Candidate sensor probe materials are discussed and chosen on the basis of melting point, high-temperature strength, and availability.

Tests are described and the results reported on the compatibility of various probe and charging metal combinations.

A special test for studying hydrogen diffusion through the probe at high hydrogen pressures and temperatures is described.

A thermal analysis of the probe was made assuming both transient and steady-state conditions. Estimates of steady-state probe temperature and variations in response time are reported. However, the severity of the hydrogen-diffusion problem makes the probe in its present state of development unsuitable for the intended application.

ERRATA

Previous issues of quarterly reports should not have NASA or Battelle number in upper right-hand corner. This final report carries the correct NASA number.

TABLE OF CONTENTS

LIST OF TABLES

LIST OF FIGURES

LIST OF FIGURES
(Continued)

LIST OF FIGURES
(Continued)

DEVELOPMENT OF A VAPOR-PRESSURE-OPERATED
HIGH-TEMPERATURE SENSOR DEVICE

by

J. R. Van Orsdel, G. E. Raines, and J. M. Allen

SUMMARY

The successful development of a vapor-pressure-operated high-temperature sensor is heavily dependent upon materials' behavior in the intended environment. The more serious aspects of the environment are temperature up to 5000 R, exposure to hydrogen at 600 psia flowing at 800 feet per second, and vibrational loads of considerable magnitude. Thus, this program was designed to find materials of construction which would be compatible with each other and the environment so that a sensor could be built which would faithfully signal environment temperature.

Tungsten, tungsten-3 rhenium, and tungsten-25 rhenium were ultimately selected as the most promising probe materials for the sensor. Bismuth and lead were found promising for charging metals. A compatibility test was devised and used to show compatibility between the probe materials and the charging metals based upon 1 hour of continuous operation at 5000 R. A second test was then conducted in a hydrogen atmosphere at 600 psia and 4500 R to determine the resistance of the probe materials to hydrogen diffusion. These tests disclosed a high rate of hydrogen diffusion through the probe walls into the probe cavity making the probe in its present state of development unsuitable for the intended application.

A signal-sensing element for attachment to the probe was designed, constructed, and characterized in a bench test.

A mathematical analysis of the stresses in the probe owing to the operating environment (not including vibration) were found to be within the maximum 500-psi allowable stress. Some control over probe stresses is exercisable through choice of the vapor pressure of the charging metal.

Thermal analysis of the probe under transient and steady-state conditions revealed that the time constant would increase as the probe temperature approaches the gas temperature. At anticipated typical conditions, the probe temperature at steady state would be about 10 per cent less than the gas temperature owing to radiative heat loss. Axial heat losses along the probe could be minimized by making the probe length at least 4 times the diameter. This sensor program was planned around a probe length of 6 times the probe diameter (1-1/2 inches).

CONCLUSIONS

Based on the results of this study the following conclusions can be made:

Lead and bismuth have favorable vapor pressures at temperatures between 4000 and 5000 R for operating a temperature sensor. Bismuth is relatively inert toward unalloyed tungsten at these temperatures under the conditions of the test program. Similarly, lead can be contained in tungsten-3 rhenium and tungsten-25 rhenium alloys. Because of a greater resistance to grain growth at high temperature, the tungsten-3 rhenium alloy would be a first-choice probe material.

Hydrogen diffusion through the atomic lattice of the probe materials is too severe to be ignored in the development of this sensor. Tests indicate that hydrogen diffusion through the probe walls is about 100 times the maximum allowable quantity. Future studies should be first directed toward the elimination of this problem.

Mechanical stresses can be held to safe limits in the probe as far as was determined during the course of the project. Complex stresses owing to a vibrational input need investigation in a critical experiment.

The response time of the probe will be most rapid during startup and will become increasingly long as the probe temperature approaches steady state at high temperatures. The length of the probe for minimum axial heat loss is about four probe diameters. Therefore, a length of 1-1/2 inches (6 diameters) is in the range for both good mechanical and thermal dimensions.

INTRODUCTION

The objectives of this project were to design, fabricate, test, and deliver an experimental model of a vapor-pressure-operated temperature sensor. The sensor was to be capable of operating continuously and survive cyclic operation from ambient temperature to 5000 R in a hydrogen atmosphere ranging from 0 to 600-psia gas pressure without decrease in performance under the following environmental conditions:

(1) Vibration — 4 g's from 10 to 500 cycles per second

*(2) Nuclear radiation — neutron flux of 5×10^{13} n/(cm^2)(sec); gamma flux of 10^{15} Mev/(cm^2)(sec)

(3) Hydrogen gas velocity — 800 ft/sec

(4) Noise level — 175 db

(5) Continuous operation for 100 hours.

Because of the high temperatures involved, a low-melting-point metal was the logical choice for the pressure-generating medium. Since the vapor pressure-versus-temperature relationship of metals above their boiling points is reasonably predictable

---

*Item eliminated from test program by decision of Sponsor prior to initiation of project.

BATTELLE   MEMORIAL   INSTITUTE

from existing data and mathematical laws, it was not deemed necessary to make exhaustive vapor-pressure studies. Rather, the essential elements of the program were (1) a review of existing data on materials for possible use as containers and charging metals, (2) computation of vapor-pressure values of charging metals at high temperatures, (3) compatibility testing of containers and charging metals over the desired temperature range, (4) computer studies of heat flow and response time, (5) test for hydrogen diffusion through probe walls into probe cavity, (6) exploratory studies of a scheme for final testing of the sensor unit at high temperature while subjected to vibratory loads, (7) design, construction, and test of the transducer readout portion of the sensor.

Although various ideas were considered for the final form of the sensor (see Appendix, Figure A-14 for initial concept), the one ultimately chosen as being simplest in operation and likely to be most immune to vibrational loads is shown in Figure 1. Consequently, experimental procedures were initiated to study the various aforementioned critical relationships.
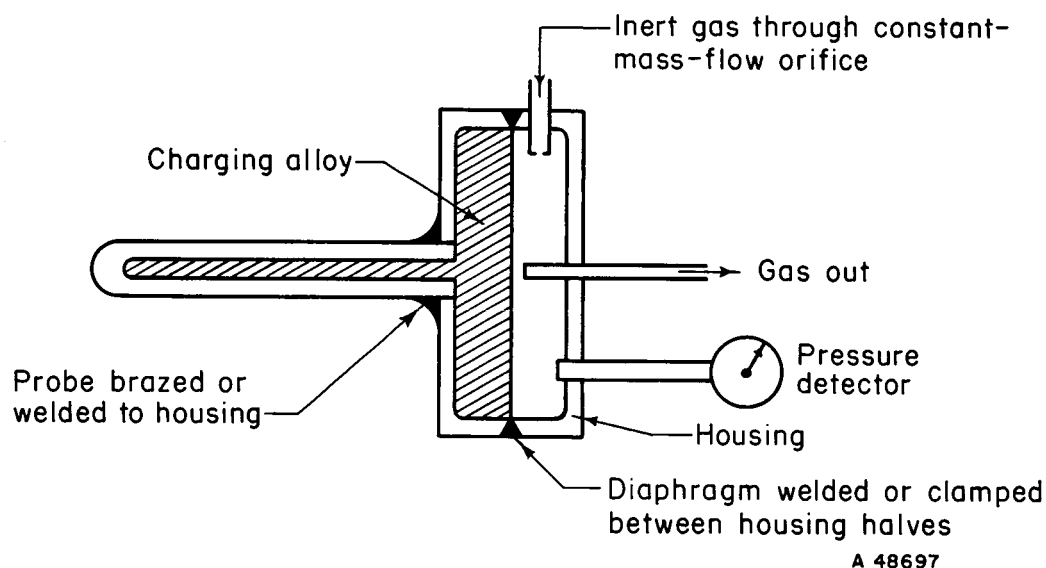
FIGURE 1. PNEUMATIC SENSOR

METALLURGY

Liquid Metals

The most important property of the liquid metal in the sensor is its vapor pressure as a function of temperature. The sensor detects the temperature of the heat source by measurement of the effect of temperature on the vapor pressure of the liquid metal. All metal parts in contact with the liquid metal must, of course, be able to resist its corrosive effect. In addition, the liquid metal should have a low melting point in order to be operative as quickly as possible when the heat source is activated.

Charging Metals

Although there are a large number of low-melting-point metals and alloys with widely varying vapor pressures, it was deemed advisable in this instance to use only a pure metal so as to avoid possible segregations in the sensor probe which would alter the vapor pressure-versus-temperature calibration.

Experimental and thermodynamically derived data on the vapor pressure of liquid metals have been published for pressures below the boiling point (where the vapor pressure equals 1 atm) of the individual metal.[*] For this program, the pressure-temperature curves were calculated for pressures appreciably higher than 1 atmosphere by extrapolation of the published data. The log of the known pressure was plotted against the reciprocal of the absolute temperature. The plot gives a straight line whenever the vapor is a monatomic gas. Thus, extrapolation was readily performed but with reservations by extending the straight line into the temperature regions of interest for this program. The pressure-temperature plots made possible by the extrapolations are shown for some low-melting metals in Figure 2. All of the pressure curves shown were for monatomic gases except for antimony. In the case of antimony, the diatomic molecule, Sb_2, predominates although appreciable amounts of monatomic Sb also exist in the gaseous state. Also, Sb_4 molecules are known to exist in appreciable quantities at lower temperatures and pressures and might form at high temperatures because of high pressure. Thus, the extensive extrapolation of vapor-pressure data for antimony is of more questionable accuracy than for the other metals. However, its use provides a preliminary comparison with the other metals.

None of the curves can be relied upon for exact calibration of the sensor because of the assumption that the vapors behave as ideal gases. However, an empirical calibration of the sensor could be made rather easily once it is assembled in final form.

The most obvious conclusion to be derived from the curves in Figure 2 is that a sensor with any one metal would be useful only over a limited temperature range. For all of the liquid metals, the lower limit for useful temperature measurement is the temperature at which the metal has a vapor pressure measurably exceeding 1 atmosphere. On the other hand, the maximum temperature of the sensor would be limited by the maximum pressure which can be withstood by the container.

The temperature range of usefulness for any one liquid metal appears to be 1200 to 1500 R. The individual metal can be chosen to place this range at various operating-temperature levels.

Of the liquid metals represented in Figure 2, the three most likely candidates were bismuth, lead, and antimony based upon their indicated pressures over the temperature range of interest, 3500 to 5000 R.

No data have been published on the corrosion characteristics of the various liquid metals at the temperatures of interest. A determination of whether lead, bismuth, and antimony attack the candidate container materials at 4000 to 5000 R enough to materially change the vapor-pressure characteristics of the liquid metal or destroy the container was a part of the research program.

---

[*]Stull, D. R., and Sinke, G. C., Thermodynamic Properties of the Elements, American Chemical Society, Washington, D. C. (1956), 234 pp.
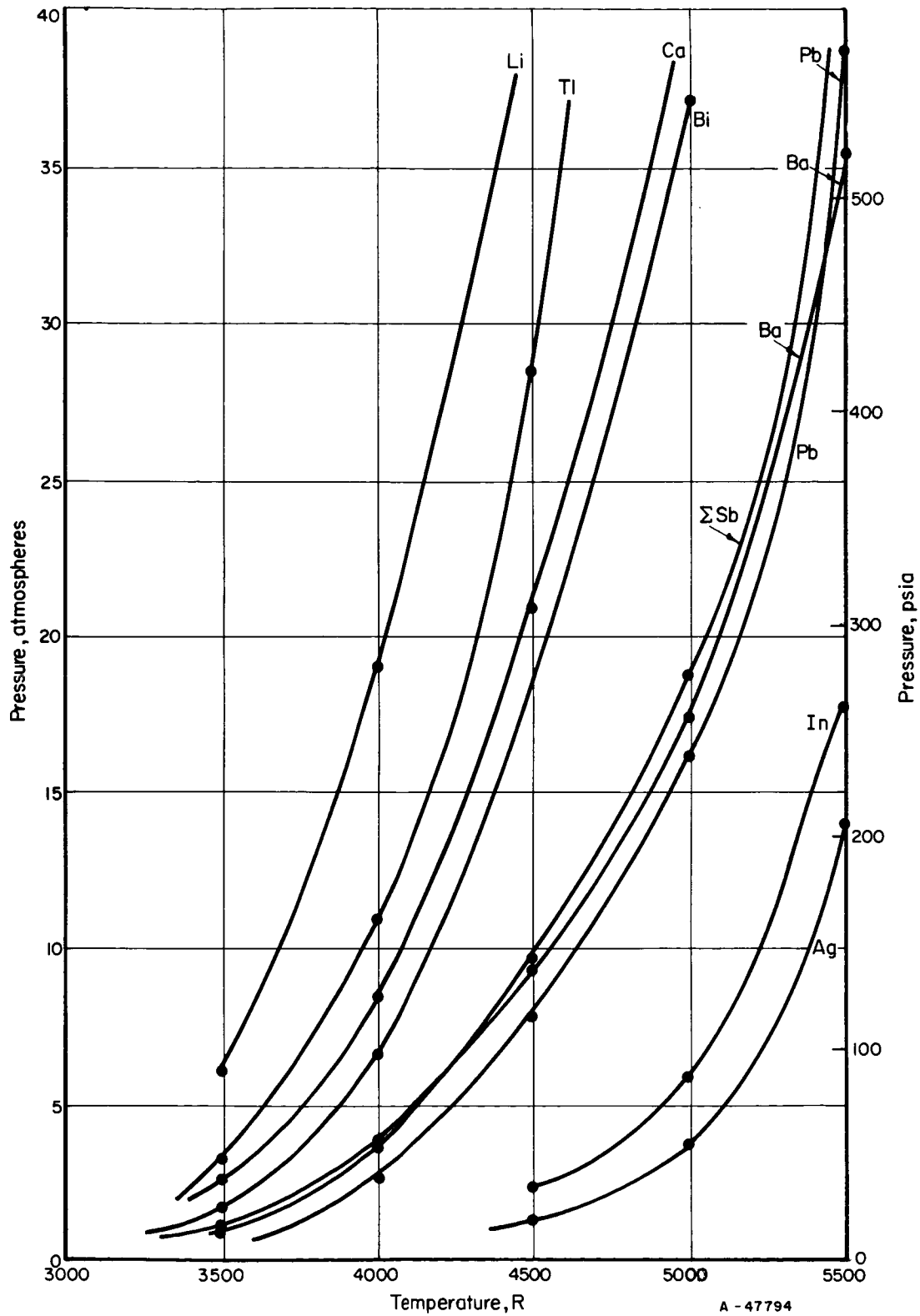
FIGURE 2. VAPOR PRESSURE OF PURE METALS BETWEEN 3500 AND 5500 R

Container Materials

The container must hold the liquid metal for the period of operation of the sensor while the vapor pressure of the liquid is at its maximum. Because the maximum temperature desired for the sensor was as high as 5000 R, only the refractory metals – tungsten, rhenium, tantalum, molybdenum, columbium – and their alloys were considered. This group of metals was further reduced to tungsten, rhenium, molybdenum and their alloys when the known affinity for hydrogen of columbium and tantalum and the resulting embrittlement was taken into account.[*]

Tungsten has the highest melting point of all the metals (6630 R) and it has been studied most intensively for very-high-temperature service.

Rhenium has the next highest melting point (6200 R) and recently has become the subject of research to discover its physical and mechanical properties. Alloys of tungsten with rhenium appear to resist the effects of high temperature on some properties more successfully than pure tungsten.

A molybdenum alloy, Mo-30W, appeared of interest as a container material for maximum temperatures somewhat below 5000 R and was evaluated in subsequent compatibility tests for this reason.

Some properties, obtained from the literature sources indicated and summarized below, reveal that a temperature-sensing probe operating at 5000 R severely taxes the strongest known metals. For a first consideration, it was prescribed that the sensor would need to operate up to 1 hour at its maximum useful temperature. Some strength and creep-rupture data for tungsten were obtained from DMIC Report 191[**] and are presented in Table 1.

TABLE 1. STRENGTH AND CREEP-RUPTURE OF TUNGSTEN
AT HIGH TEMPERATURES

Temperature, R	Tensile Strength, psi	Maximum Stress for Rupture in 1 Hr, psi	Maximum Stress for Creep of ~ 0.2 %, psi
3500	5,000-30,000	9,000-17,000	3,000-6,000
4000	4,000-29,000	< 5,000	?
4500	3,000-14,000	1,000-4,000	< 3,000
5000	2,500-9,000	1,000-3,000	< 3,000
5250	2,500-7,000	Few hundred to 2,100	?

The tensile strength of tungsten depends to a considerable extent on the purity, shape, size, and fabrication history of the tungsten. However, this would only account

[*]Rare Metals Handbook, 2nd Edition, Reinhold Publishing Company, pp 164 and 499.
[**]Schmidt, F. F., and Ogden, H. R., "The Engineering Properties of Tungsten and Tungsten Alloys", DMIC Report 191, Battelle Memorial Institute (September 27, 1963).

for a small portion of the spread in observed tensile strengths in the above tabulation. The most important variation is in the strain rate of the tensile test itself. For example, at 3500 R, the tensile strengths of tungsten range from 6000 psi at a very low strain rate of 0.002 inch per inch per minute to 25,000 psi at the high strain rate of 20 inches per inch per minute. At 4500 R, the strength ranges from 3,000 to 13,000 over the same range of strain rates.

The modulus of elasticity is of some importance in determining the reaction of the sensor to its expected high-vibration environment. Some data from DMIC Report 191 for unalloyed tungsten are tabulated below:

Temperature, R	Modulus of Elasticity, 10^6 psi
Room temperature	50
3000	28
3500	15
4000	7

The tungsten-3 per cent rhenium alloy shows considerable improvement over tungsten with regard to high-temperature strength (DMIC 191). For example, it shows a tensile strength of over 50,000 psi at about 4000 R on wire tested at 0.4 inch per inch per minute. This is about 2-1/2 times the strength of unalloyed tungsten at the same temperature. Much of this additional strength arises from a resistance to recrystallization. The normal recrystallization temperature is 5890 R (3 minutes) for heavily-drawn wire. The stress-relief temperature is 4520 R (3 minutes).

Increasing the rhenium content to 5 per cent, the tensile strength of the cold-worked wire at 4000 R is increased still further to over 60,000 psi.

The tungsten-26 per cent rhenium alloy is characterized by especially high ductility, particularly when it is made as a high-purity, arc-cast alloy.

Some additional property data, obtained from other sources are presented in Table 2.

TABLE 2. HIGH-TEMPERATURE PROPERTIES OF SOME REFRACTORY METALS

Material	Temp, R	Stress, psi	Time to Effect 2% Strain, hr	Time to Rupture, hr	Elongation in 1-inch Gage Length, %
W[a]	5172	1000	--	25.1	5
Re[b]	5172	1000	~ 3	~ 20	~ 14
W-25Re[b]	5172	1000	1	3	10
W-3Re	5172	1000	--	--	--
Ta-10W[b]	5172	1000	0.1	1.5	120

(a) "High Temperature Materials Program", Progress Report No. 35, Part A, USAEC Contract AT (40-1)-2847, p 16, Table 2.2.
(b) "Stress-Rupture and Creep Properties of Refractory Metals to 2800 C", General Electric Company USAEC Contract AT (11-1)-171.

Additional information was gathered from the literature on tantalum and columbium alloys and is reported in the "First Quarterly Report" of this program but did not show enough promise to warrant further consideration in subsequent studies.

Consequently, as the result of the preceding materials studies, five metals were selected as candidates for the sensor probe. These materials were unalloyed tungsten, unalloyed rhenium, molybdenum-30 per cent tungsten, tungsten-3 per cent rhenium, and tungsten-25 per cent rhenium. These materials were obtained from suppliers in the form of swaged and ground 1/4-inch-diameter rod. Specimens used in the materials-evaluation studies were cut from the rods and drilled by electrical discharge machining (EDM) to provide thick-walled tubular forms representative of the probe. Tubing of this type in the materials of interest was not readily available from industry. There is little doubt that without the EDM process for machining difficult materials, there would have been considerable delay in obtaining simple tubular shapes for this project.

A 1/4-inch-diameter tube with a 1/8-inch-diameter bore was arbitrarily chosen as a probe geometry and then its suitability confirmed in the following manner.

The static stresses imposed on the specimens during compatibility testing are a result of the internal liquid-metal vapor pressure and the external furnace-atmosphere pressure (1 atm). However, the expected application of the sensor specifies an external pressure of 600 psia. Therefore, it is interesting to calculate static stresses arising in the probe owing to these two conditions.

The static stresses are calculated by treating the specimen as a thick-walled cylinder and applying Lamé's solution[*]:

$$\text{Max } S_t = \frac{P_1(r_1^2 + r_2^2) - 2P_2 r_2^2}{r_2^2 - r_1^2} \quad ,$$

where

$\text{Max } S_t$ = maximum circumferential stress

P_1 = internal pressure

P_2 = external pressure

r_1 = radius of specimen bore, 1/16 inch

r_2 = maximum specimen radius, 1/8 inch.

Max S_t will be positive (tension) or negative (compression), depending upon the relative values of P_1 and P_2. The other stresses arising from the gas pressures are S_r, which is a radial stress, and S_s, which is a shear stress. S_r and S_s were both found by calculation to be of secondary importance relative to max S_t; therefore, they will be ignored for the present.

Calculated values of Max S_t experienced by the specimens (1/4-inch OD x 1/8-inch ID) during compatibility testing and those that could be expected to arise from an external pressure of 600 psia are given in Table 3.

---

[*]Resistance of Materials, Seely, Third Edition, p 388.

TABLE 3. STATIC STRESSES (MAX S_t) OWING TO INTERNAL AND EXTERNAL GAS PRESSURES

Charging Metal	Exposure Temp, R	Vapor Pressure (P_1), psia	Max S_t[a], psi	
			$P_2 = 14.7$	$P_2 = 600$
Bi	4000	97	122	-1430
	4500	277	422	-1030
	5000	531	848	-704
Sb	4000	51	46	-1500
	4500	142	198	-1355
	5000	277	422	-1030
Pb	4000	40	27	-1520
	4500	117	240	-1395
	5000	240	361	-1190

(a) Positive values of stress are tension, negative values are compression.

Examination of Table 3 reveals that the static stresses in the probe will be largest and compressive when the external atmosphere is 600 psia. This is thought to be a favorable circumstance providing the compressive stress is not sufficient to collapse the probe. It is natural to assume that a more favorable stress level could be achieved by thickening of the probe walls. However, a few sample calculations of stress for different wall thicknesses and bore diameters quickly reveal that a geometry in which the wall thickness equals the radius of the bore is just about the optimum condition that can be obtained. The following examples are presented for clarification, using 117 psia for P_1, the internal pressure.

Bore Diameter, inch	Probe Diameter, inch	External Pressure, P_2, psia	Max S_t, psi
1/8	1/4	14.7	240
1/8	1/4	600	-1395
1/16	1/4	14.7	101
1/16	1/4	600	-1145
1/8	3/8	14.7	113
1/8	3/8	600	-1200

It is readily seen from the above examples that reducing the bore diameter or increasing the external diameter of the probe has only a negligible effect on lowering the compressive stresses resulting from the high external pressure of 600 psia. Only equalization of internal and external pressures can eliminate stresses of this type in the probe. For this purpose, bismuth (Table 3) would be the best choice of a charging fluid, if compatibility with the container is satisfactory.

Creep is not expected to differ greatly in compression from that in tension because of rapid annealing at the high temperatures involved.

Compatibility Tests

The ability of the probe to resist corrosive attack by the liquid metal which it contains was of prime importance. Therefore, a program of compatibility testing was undertaken to establish the relative merits of the candidate probe materials when containing lead, bismuth, and antimony at temperatures as high as 5000 R. The specimen exposure time was 1 hour. The specimen heating apparatus is shown in Figure 3. A megatherm induction heating machine operating at 500 kc and voltages up to 16000 was used as the power supply.

The induction coil shown in Figure 3 was later replaced by a coil consisting of 11 flattened turns of 1/4-inch-diameter copper tubing expanded to a coil length of 2-3/8 inches. The inside diameter of the coil was 3/4 inch. This new coil made specimen heating to 5000 R possible with about 3600 volts. Previously voltages ran as high as 9000 and arcing between coil and specimen was a problem. A 3-inch-diameter fused quartz tube seen in Figure 3 served as a protective envelope through which hydrogen was passed during specimen heating.

Specimen temperature was read by a Leeds and Northrup optical pyrometer sighted, with the aid of a mirror, onto the induction-heated end. Temperature readings were taken every 5 minutes during a run and it was found possible to maintain the specimen temperature within about ± 50 degrees of the intended value. Fluctuations were associated with some instability in the power supply. Corrections for emissivity of tungsten and transmission of the quartz were applied to the temperature readings.

Two styles of specimens were used in this phase of the program. Figure 4 depicts the initial configuration and Figure 5 the later revision. The change in style was made in the interest of material economy and did not influence the results of experimentation in any way.

The specimen shown in Figure 5 was 1-1/2 inches long with a 1/8-inch-diameter hole drilled by EDM 1-1/8 inches deep. The support rod was 4-1/2 inches long. The heat shield and EB (electron beam)-welded plug arrangement was used for closure just the same way as shown in Figure 4. The heat shield was found to be necessary to prevent rapid evaporation of the charging metal by the intense heat radiation from the internal end of the plug during EB welding.

Prior to fabrication of the specimens, the machined and drilled parts were washed in CCl_4 then heated to 2000 F for 15 minutes in hydrogen to provide thoroughly clean surfaces.

Tantalum was also tested as a container for lead, antimony, and bismuth because it was thought to have promise as a material of construction in the signal end of the sensor. It was not heated during cleaning as were the other specimens. The tantalum specimens were packed in titanium chips and protected with an argon atmosphere while being exposed to 2460 R in a Globar-heated Inconel-tube furnace.

Compatibility test data for all specimens are tabulated in Table 4. Photomicrographs of the metal-liquid metal contact zones are displayed in the Appendix, Figures A-1 through A-13 and A-15 through A-28. From the results of the compatibility tests it was determined that W; Bi, W-3Re; Pb and W-25Re; Pb showed promise as suitable probe-charging-metal combinations.

BATTELLE MEMORIAL INSTITUTE
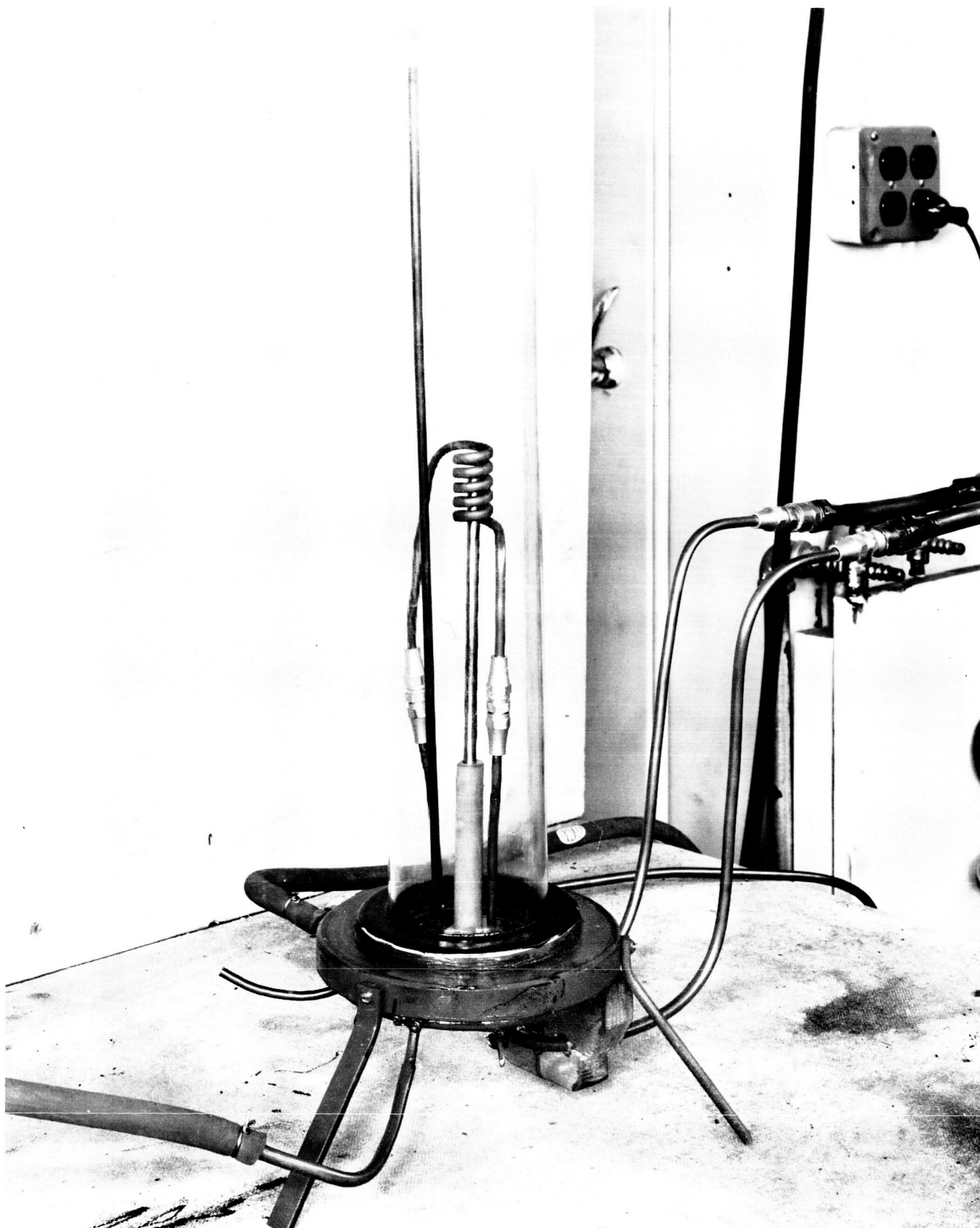
FIGURE 3.   INDUCTION FURNACE FOR SAMPLE HEATING

BATTELLE   MEMORIAL   INSTITUTE

N10756
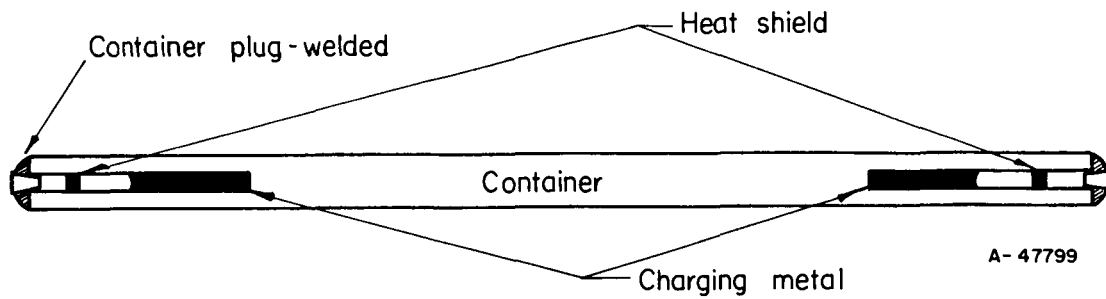
FIGURE 4. CROSS SECTION OF SPECIMEN USED IN COMPATIBILITY
TESTS OF CONTAINER VERSUS CHARGING METAL

Full scale.
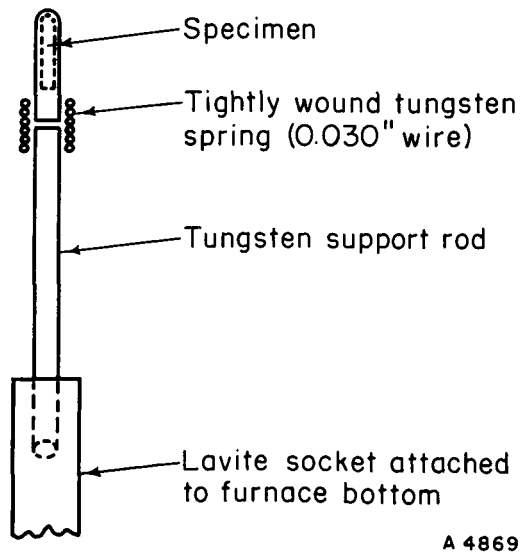
FIGURE 5. REVISED SPECIMEN AND METHOD OF HOLDING
FOR HIGH-TEMPERATURE TESTING

TABLE 4. DATA SUMMARY OF COMPATIBILITY TESTS

Specimen	Material	Exposure Temp, R	Exposure Time, min	Results
1	Ta; Pb	2460	60	Minor reaction, no leaking
2	Ta; Sb	2460	60	Some reaction, no leaking
3	Ta; Bi	2460	60	No reaction, no leaking
4	Mo-30W; Pb	4000	60	No reaction, no leaking
5	Mo-30W; Bi	4000	60	Slight grain-boundary reaction, no leaking
6	Mo-30W; Bi	4500	30	More grain-boundary penetration; no leaking, container expanded by pressure
7	Mo-30W; Pb	4500	60	Some reaction, no leaking
8	W; Bi	4500	60	No reaction, no leaking
9	W; Bi	5000	10	No reaction, leak at weld
10	W; Pb	4500	60	Moderate reaction, no leaking
11	W; Pb	4700	25	Severe reaction, leaking
12	W; Sb	4500	60	Minor reaction, no leaking
13	W; Sb	5000	15	Minor reaction, leaking
14	Mo-30W; Sb	4500	5	Specimen ruptured
15	W-3Re; Bi	4500	3	Specimen ruptured
16	Repeat	No. 15		Same results
17	W-3Re; Sb	4500	60	No leaking
18	W-3Re; Sb	5000	5	Specimen ruptured
19	W-3Re; Pb	4500	60	No leaking
20	W-3Re; Pb	5000	60	Ditto
21	W-25Re; Pb	4500	60	"
22	W-25Re; Pb	5000	60	"
23	W-25Re; Sb	4500	60	"
24	W-25Re; Sb	5000	60	Sample bulged 0.006 inch on diam, or 2.4 per cent
25	W-25Re; Bi	4500	60	No leaking
26	W-25Re; Bi	5000	50	Sample bulged about 50 per cent in diam, then ruptured
27	Re; Pb	5000	60	No leaking
28	Re; Bi	5000	60	No leaking

HYDROGEN DIFFUSION STUDIES

Before the temperature sensor could be constructed and put into use with confidence in its output signals, it was necessary to verify that the probe would be impermeable by hydrogen. Dalton's law states that the total pressure of a mixture of gases is equal to the sum of the individual pressures that would exist if each gas occupied the entire container by itself. Therefore, it can readily be seen that an influx of hydrogen over a period of time would change the calibration of the instrument. Also, an additional complicating factor influencing calibration is that one of the gases, the metal vapor, is a condensable gas when below its critical temperature. Therefore, hydrogen diffusing into the probe cavity over a period of time at steady temperature might conceivably displace all of the metal vapor giving an entirely different temperature response signal than that of the original calibration.

Furnace Construction

In this phase of the research, it was necessary to conduct the hydrogen diffusion studies under conditions simulating the probable end use. Thus a special furnace capable of temperatures up to 5000 R, while containing hydrogen at 600 psia, was built. The furnace was heated by induction. The first furnace cracked owing to thermal stresses and temperatures were limited by the tendency of the quartz tube envelope to become conducting at elevated temperatures. This caused arcing between the induction coil and the quartz tube. Subsequently, alterations in shape of the tungsten furnace and water cooling of the quartz tube corrected the problems and the experiments were carried out successfully.

Figure 6 is a schematic layout of the diffusion-test setup. The tungsten furnace was 7 inches long and 1 inch in diameter. The bore was 9/16 inch in diameter and was 6-1/2 inches deep. The surrounding fused quartz envelope was 1-13/16-inch ID by 2-inch OD and 12 inches long. Hydrogen was passed through the quartz tube to protect the hot tungsten furnace from the atmosphere.

Test Procedure

The specimens used in the hydrogen diffusion studies were made from 1/4-inch-diameter rod of the materials to be evaluated. They were 3/4 inch long with a 1/8 inch hole drilled 5/8 inch deep from one end (see Figure 6). Cleaning procedure was the same as used with the compatibility specimens. The materials were tungsten, tungsten-3 rhenium, and tungsten-25 rhenium. All were products of powder metallurgy which had been sintered, swaged, and ground to final finish by commercial suppliers. Figures A-28 through A-30 in the Appendix are representative photomicrographs of the materials in the as-received condition. Densities of the materials were found to be essentially 100 per cent of theoretical by the water-submersion technique. The dark specks appearing in the photomicrographs resemble small oxide inclusions and are not thought to be detrimental for this application.

Mirror

Optical pyrometer

Fused quartz tube
2" OD x $1\frac{13}{16}$" ID x 12" long

Water flood cooling for tube

Mercury column pressure-relief system

Pressure gage

High-pressure H_2 from storage

Induction coil ($\frac{1}{4}$" copper tube)

Specimen held to support by 0.030"-tungsten wire spring support

Heat shield

Tapered plug EB welded

Hollow tungsten support rod

High-pressure chamber (600 psi H_2)

Tungsten furnace

$\frac{1}{16}$-inch space packed gastight

H_2 to furnace at 600 psia

Low-pressure H_2 purge

Lavite collar cemented to base

H_2 out

Lavite base

Water in

Water out

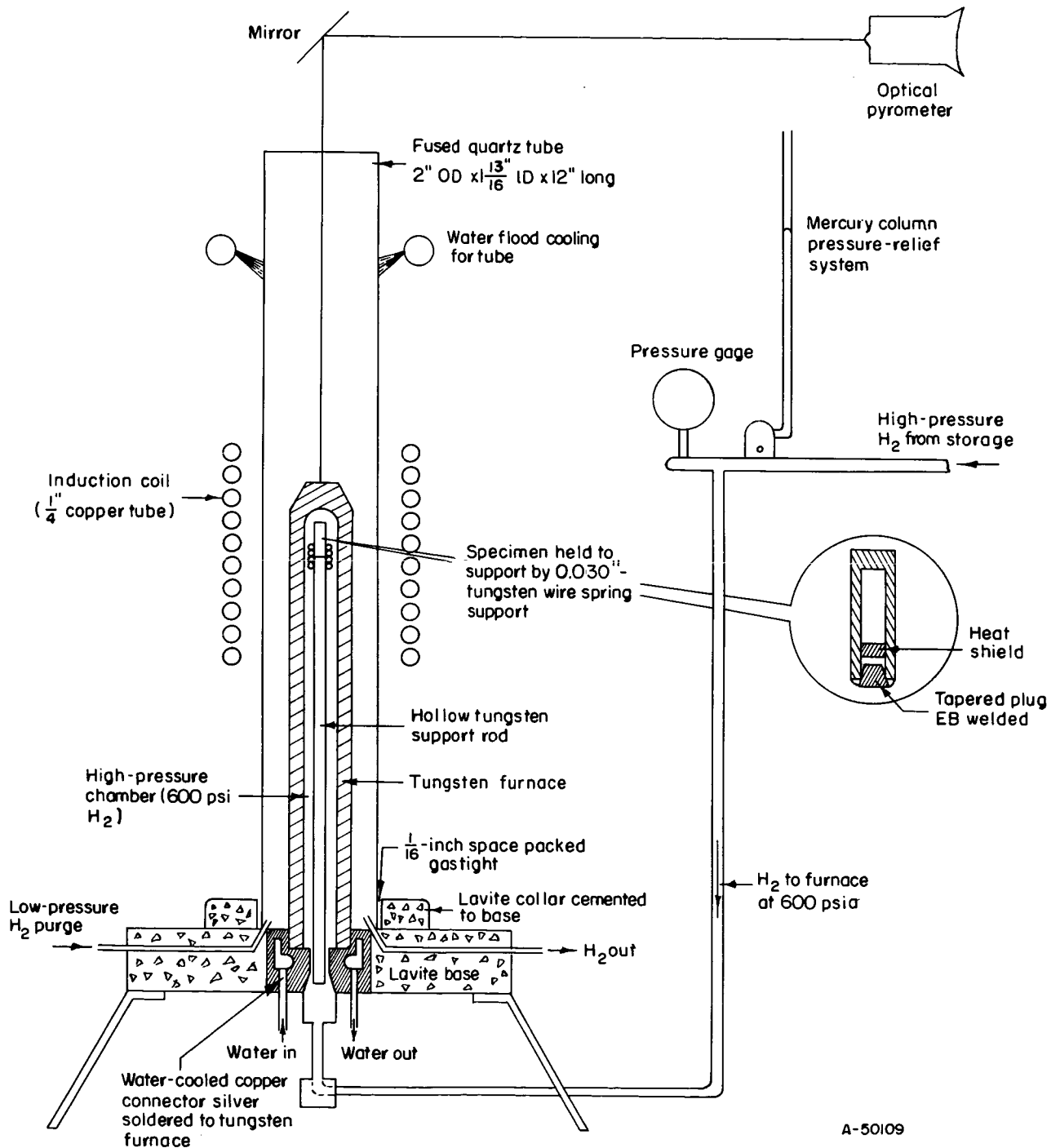Water-cooled copper connector silver soldered to tungsten furnace

A-50109

FIGURE 6.   HIGH-PRESSURE HYDROGEN-ATMOSPHERE FURNACE

The plan for evaluating the resistance of the materials to hydrogen diffusion was to heat the evacuated specimens to temperature for 1 hour in the presence of hydrogen at 600 psi. Subsequent vacuum-fusion analysis of the specimens would reveal hydrogen accumulation in the specimen cavity. In order to differentiate between hydrogen residing in the metal and free hydrogen in the cavity, four steps were taken with each material with duplicate specimens run at each step. Thus a total of 8 specimens were planned for each of the three materials. The procedures were as follows except that Procedure 4 was dispensed with for the W-25Re alloy. Also, venting, as in Procedure 3, was not done on this alloy for reasons of obtaining a greater number of similar specimens for H_2 analysis.

Procedure 1: Evacuate and seal by electron-beam (EB) welding after cleaning; hold for H_2 analysis.

Procedure 2: Evacuate and seal by EB welding after cleaning, then heat for 1 hour in 600 psia H_2 at 5000 R, analyze for H_2.

Procedure 3: Same as Procedure (2), except cut sample open to allow any H_2 present to escape before analysis.

Procedure 4: Place appropriate charging metal in sample, evacuate and seal by EB welding, then heat and analyze for H_2 as in Procedure (2).

By stipulating that the maximum amount of error in probe pressure at 5000 R by the presence of hydrogen be limited to +10 psi (32 R if lead is used)[*], it was possible to estimate the amount of hydrogen that could be tolerated in the sample cavity. The hydrogen pressure which would cause a 32-degree error in temperature at 5000 R induces an approximate error over the full-scale temperature range as follows:

Probe Temperature, R	Partial Pressure of Lead, psia	Partial Pressure of Hydrogen, psia	Error in Temperature Indication, R
492	$\simeq 0$	≈ 1	--
3500	$\simeq 1$	7	--
4000	40	8	+72
4500	115	9	+48
5000	240	10	+32

Employing the ideal gas laws, for the stipulated conditions, the maximum pressure of hydrogen that could be tolerated within the sample cavity at standard conditions was calculated to be:

$$P_1 = \frac{T_1 P_2}{T_2} = \frac{492 \times 10}{5000} = 0.985 \text{ psia.}$$

Since the H_2 analysis was reported in milliliters at standard conditions, this value of pressure was converted to milliliters and related to the volume of the sample cavity. The allowable maximum of H_2 content in standard milliliters would be 0.985/14.7 x 100 = 6.7 per cent of the sample-cavity volume. Unfortunately, hydrogen was found to be much more aggressive than this in permeating the materials under study.

---

[*] Temperature error was estimated from the curve for lead, Figure 2.

The cavity volume within the specimens was determined, after evacuation and electron-beam welding but before high-temperature exposure, by calculation from measurable values of specimen weight and density. Thus the cavity volume is

$$V_c = \frac{(\text{dry weight} - \text{wet weight})}{\text{density of } H_2O} - \frac{\text{dry weight}}{\text{theoretical density of the alloy}} \quad .$$

The net hydrogen content of the cavity is assumed to be the total H_2 content minus the average content of two control specimens showing the highest H_2 content.

Knowing the hydrogen content of the cavity and the cavity volume, it is possible to calculate the probable pressure level, P, reached by the hydrogen in the specimen cavity during the 1-hour high-temperature run.

$$P = \frac{14.7 \times V_1}{V_c} \times \frac{T_2}{492^*} \quad ,$$

where

V_1 = net milliliters of hydrogen found in the specimen as a result of the high-pressure temperature exposure

V_c = cavity volume in cubic centimeters assumed equivalent to milliliters

T_2 = specimen exposure (temperature, degrees R)

*492 is the magnitude of standard temperature in degrees R

Table 5 summarizes the results of the diffusion studies.

The results of the hydrogen diffusion studies indicate a decided influx of hydrogen into the cavity. Those specimens having very low H_2 contents are suspect of having leaked before analysis. The specimens having H_2 contents indicative of pressures greater than the external pressure of 600 psi at the exposure temperature are suggestive of osmotic effects familiar in systems involving semipermeable membranes. In these experiments, atomic hydrogen would be present because of the high temperatures involved. Solution of the atomic hydrogen into the surface of the metal might be of sufficient vigor to constitute a driving force capable of building the excessive internal pressures observed. A case in point is the blistering of steel at ordinary temperatures when subjected to pickling or electroplating processes where atomic hydrogen is available to the metal surface. Such blistering is suggestive of the creation of high pressures from permeation by hydrogen.

TABLE 5. RESULTS OF HYDROGEN DIFFUSION STUDIES FOR 1-HOUR EXPOSURES

Specimen Identification[a]	Exposure, Temp, R	Exposure H_2 Pressure, psia	Net H_2 Content, ml, STP	Specimen Cavity Volume, cc	Probable Internal H_2 Pressure at Exposure Temp, psi
W-1	None	None	0.017	0.113	None (control)
	None	None	0.009	0.097	None (control)
W-2	3900	250	0.042	0.105	47
	4000	600	0.569	0.110	620
W-3	3900	250	0.013	0.117	Vented before analysis
	4000	600	0.029	0.104	for additional control
W-4[b]	4500	600	0.382	0.098	530
	4500	600	0.424	0.092	630
3D-1	None	None	0.033	0.099	None (control)
	None	None	0.031	0.109	None (control)
3D-2	4500	600	0.07	0.089	0
	4500	600	0.601	0.098	825
3D-3	4500	600	0.099	0.103	Vented before analysis
	4500	600	0.059	0.107	for additional control
3D-4[c]	4500	600	0.340	0.098	470
	4500	600	0.368	0.098	500
25D-1	None	None	0.014	0.089	None (control)
	None	None	0.020	0.094	None (control)
25D-2	4500	600	0.571	0.102	750
	4500	600	0.566	0.086	890
25D-3	4500	600	0.600	0.101	800
	4500	600	0.563	0.090	840

(a) W is symbol for unalloyed tungsten. 3D is symbol for tungsten-3 rhenium alloy. 25D is symbol for tungsten-25 rhenium alloy.
(b) Specimens contained 0.3 gram of bismuth.
(c) Specimens contained 0.4 gram of lead.

ENVIRONMENTAL DYNAMIC EFFECTS ON PROBE

Steady-State Bending Loads

The aerodynamic drag on the probe during operation tends to bend the probe in a downstream direction. This load was calculated as being 3/4 lb distributed over the 1-1/2-inch length of the 1/4-inch-diameter probe with a gas density of 6.98×10^{-4} slugs/ft^3 and a transverse gas velocity of 800 ft/sec. The corresponding stress at the root of the probe was calculated as being 167 psi, tension on the upstream side and compression on the downstream side. As this is within the strength limitations of tungsten, even at elevated temperatures, no probe bending due to aerodynamic forces is anticipated in the 800-ft/sec-velocity region. Should the probe be used in higher velocity regions, the bending moment and associated stress level will increase as the square of the velocity. Caution must be exercised, therefore, to prevent probe installation in regions of appreciably higher gas velocity.

Oscillations

The likelihood of probe oscillations caused by or coupled with exterior gas dynamic effects was investigated briefly. The possibility of both von Karman vortex shedding and higher frequency shedding was considered. Of particular concern is the case where vortex shedding frequency couples with a natural frequency of probe vibration, such that the gas stream supplies sufficient energy to the probe to maintain large-amplitude transverse oscillations. Thus, a comparison must be made between natural frequency of oscillation of the probe and vortex shedding frequency.

Assuming a 2500 R tungsten probe of 1/4-inch diameter, cantilevered, and 1-1/2 in. long, the natural frequency of the first-mode oscillation is about 2500 cycles per second. As the probe is heated to 4500 R, the natural frequency falls off to about 2000 cycles per second. No higher modes of vibration are considered significant for a probe only 6 diameters in length.

Next, we must look at the gas flow conditions which might drive the probe at these frequencies. In the von Karman phenomena, vortices are shed from the downstream side of the probe. The frequency, f, is associated with probe diameter, d, and gas velocity, V, as follows: $\frac{fd}{V} = 0.21 =$ Strouhal number. Thus, the critical velocity to induce oscillations at 2000 cycles per second is

$$V_{crit} = \frac{fd}{0.21} = \frac{2000\frac{cycles}{sec} \times \frac{1}{48} ft}{0.21} \cong 200 \text{ ft/sec} \quad .$$

Similarly, at the lower temperature, the critical velocity would be about 250 ft per sec. As the lowest steady-state gas velocity anticipated in the proposed application of this probe is over 800 ft/sec, no prolonged coupling with von Karman-type vortices is anticipated. Short-duration coupling during transient starting operation of the probe

might occur, but in this period the temperature of the probe should be appreciably lower than 2500 R, and, thus, the available strength should be correspondingly higher. Thus, no probe vibrations coupled with von Karman shedding are expected to last long enough to induce failure, even during this startup period.

It has recently been recognized[*] that initially vibrating obstacles, such as this probe, can produce vortices at the forced frequencies which do feed energy back into the vibrating system. The available literature has been reviewed,[**] but while confirming the actuality of such a phenomenon, they do not set forth the needed information for either predictive or corrective procedures. The literature suggests that the Strouhal number below which the phenomenon occurs is a function of the logarithmic decrement of damping of the probe in free vibration and a group of the form $\rho V^2/m_t f^2$, where ρ is the fluid density and m_t is the mass of the probe per unit length. Sebald and Nobles[***] indicate that the maximum deflection amplitude in the oscillation, transverse to the flow direction, may be about the same as the static deflection of the probe in the direction of flow as a result of drag forces. Thus, even if this vibration should be sustained, appreciable increases in stress level over that associated with steady-state deflection are not considered likely.

Stress Considerations

There are several sources of loading on the metal probe. Included are

● Internal gas pressurization on the cylinder

● External gas pressurization on the cylinder

● Plug-type axial gas loading

● Bending due to aerodynamic forces.

These were analyzed briefly considering the probe to be 1-1/2 inches long, 1/8-inch ID, 1/4-inch OD, immersed in a 600-psi hydrostatic pressure, with an internal pressure between 600 psi and zero. The maximum net stress value encountered is below 1000 psi. Figure 7 portrays the triaxial stress system by which the analysis was made.

The maximum shear (i.e., maximum difference between absolute orthogonal stress) was similarly found to be below 500 psi. These maximum values occur at the relatively cool base of the probe, with lower values being obtained near the tip where the maximum temperatures would be encountered. Thus, it was concluded that any material retaining 1000-psi strength at operating temperatures would be satisfactory (see Appendix pp A-17 — A-22 for analysis).

---

[*]Ozker, M. S., and Smith, J. O., "Factors Influencing the Dynamic Behavior of Tall Stacks Under Action of Wind", Trans. ASME, p 1386 (1956).

[**]Putnam, A. A., "Flow-Induced Noise and Vibration in Heat Exchangers", presented at ASME Annual Winter Meeting, November-December, 1964, New York, N. Y.

[***]Sebald, J. F., and Nobles, W. D., "Control of Tube Vibration in Steam Surface Condensers", Proceedings of American Power Conference, Vol XXIV, 630 (1962).
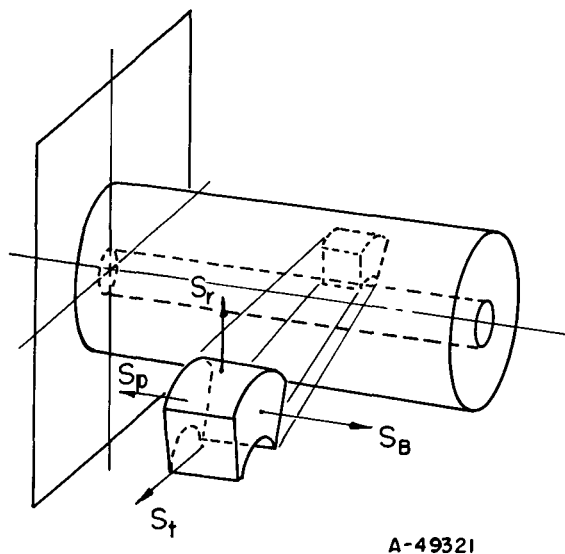
A-49321

FIGURE 7. STRESS CONFIGURATION

DIAPHRAGM TRANSDUCER DESIGN

The mechanical output of the vapor-pressure element is not sufficient to actuate directly a control mechanism. It must be used to actuate some type of transducer whose output can in turn be used to perform the control function. A diaphragm-type pneumatic amplifier was chosen as the simplest device to satisfy the requirements of adequate power output, operation in a nuclear environment, and utilization of pressurized hydrogen as an available power source.

A preliminary analysis of a diaphragm design was considered in which the diaphragm was (a) sufficiently rugged to withstand a pressure differential of 20 atmospheres and (b) sufficiently rigid that the natural frequency exceeded 500 cycles/sec, thus preventing resonance with possible imposed vibrations. With this approach, the vapor pressure is essentially balanced by the spring constant in the diaphragm. The central deflections available with such diaphragms were unacceptably small, such that poor transducer resolution would be obtained.

Therefore, it was decided to drop the requirement of high resonant frequency and instead to utilize a thin, small diaphragm. The diaphragm is thus effectively limp, the vapor-pressure balancing force is supplied by the output gas pressure, and the output pressure becomes essentially independent of the diaphragm properties.

Assuming that the element is filled with lead, at 5000 R the output will be about 0.4 psi/R, and at 3500 R, about 0.0375 psi/R. To make any error due to the diaphragm deflection small compared with the desired accuracy of ±50 R required that the output be in error by not more than about ± 2 psi. Hence, the pressure difference needed to full stroke the diaphragm should be of this order.

The requirement of a relatively small pressure difference to stroke the diaphragm means that a thin diaphragm must be used, and the necessary ruggedness must be provided by a diaphragm stop or support to protect the diaphragm from excessive deflections.

The actual choice of diaphragm diameter and thickness was made by imposing an active stroke of 0.008 inch at a stress level of 16,000 psi (approximately 1/2 the yield stress of stainless steel), at a differential pressure in the range of 2 psi and limiting the diameter to a value of less than 1.5 inches. The resulting values were a diameter of 1.07 inches and a thickness of 0.005 inch. To provide overpressure protection, it was decided to limit the actual diaphragm displacement to 0.004 inch from the neutral position. This stroke is sufficiently large to permit machining the transducer to reasonable tolerances.

Figure 8 is a cross-sectional view of the transducer developed for this program. Two large rings are shown which, with the six bolts, hold the two halves of the transducer together. In any final or flight-weight design, the two sections could be welded together where shown to eliminate the need for the rings and bolts. The vapor bulb or probe connection is shown on the right. The passage between the probe and the diaphragm chamber is reduced to 0.010-inch diameter for a 1/4-inch length. This restriction serves to dampen any flow oscillations which might be associated with diaphragm oscillations. Although the probe attachment to the transducer was by means of threads in the laboratory model, welding could be used in the final design.

The gas supply port is shown on the left. The high-pressure gas is supplied to the diaphragm chamber through an orifice 0.0135 inch in diameter. The gas outlet port in the center of the probe is shown in detail in the insert on Figure 8. Diaphragm oscillations were sometimes encountered in the laboratory calibration study when a single-ported outlet was used. No oscillations were observed with this multiported outlet.

Figure 9 shows the results of a calibration of this transducer using 800-psi nitrogen as the supply gas, and mercury on the probe side of the diaphragm. The calibration was conducted at ambient temperatures. The output pressure, i.e., pressure read through the readout port, is always slightly higher than the input pressure or liquid-metal pressure due to the reduced pressure in the gas-outlet-port region of the diaphragm. As the input pressure was reduced to zero, the output pressure dropped linearly to 5 psi.

<u>THERMAL ANALYSIS</u>

<u>Response</u>

An inherent characteristic of the temperature sensor is its thermal response (desired time constant of about 1/2 second). A knowledge of this characteristic, therefore, was sought through the application of a simplified transient analysis to provide early estimates of the importance of various parameters. Subsequently more refined
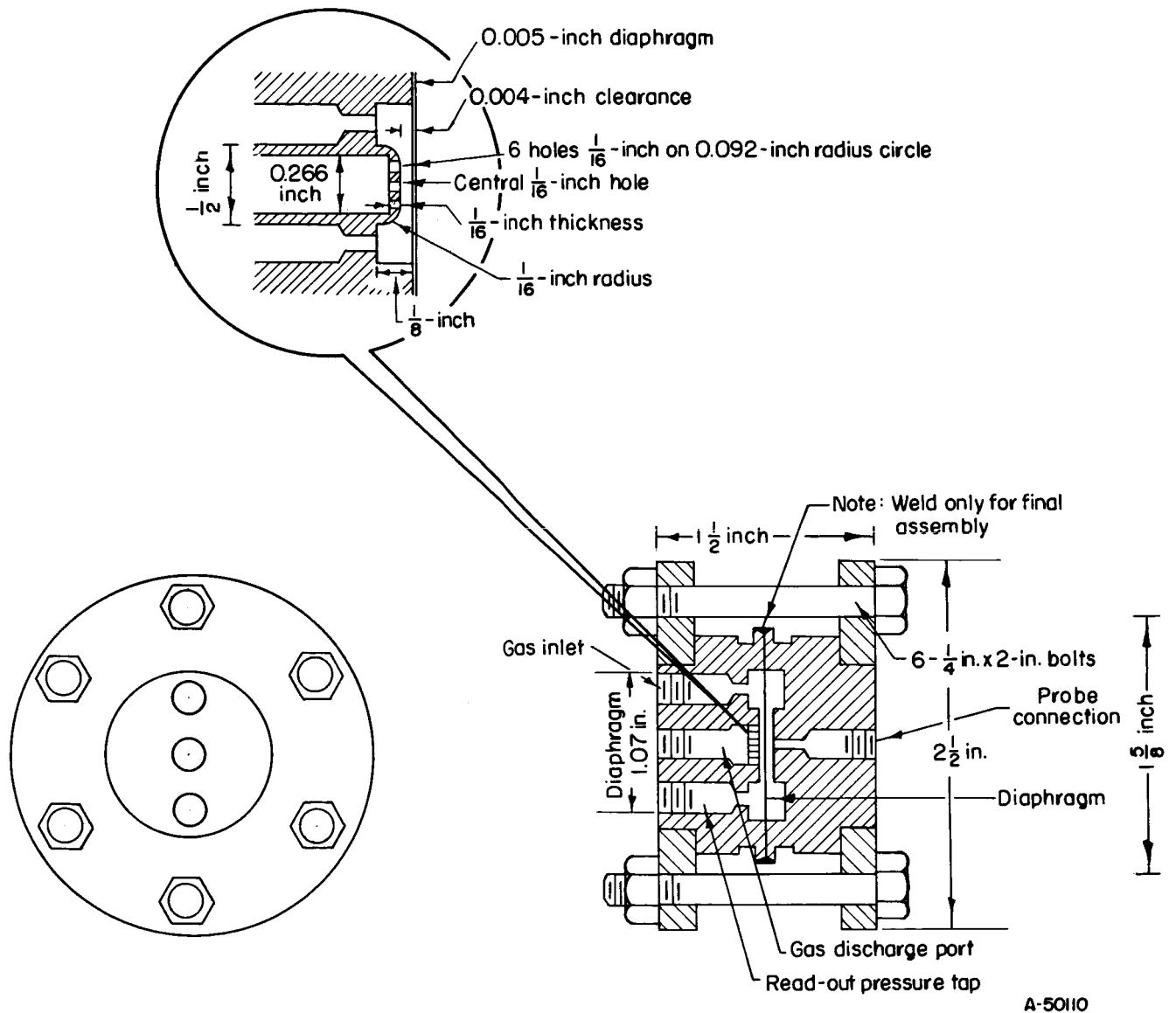
FIGURE 8.   VAPOR-PRESSURE TRANSDUCER
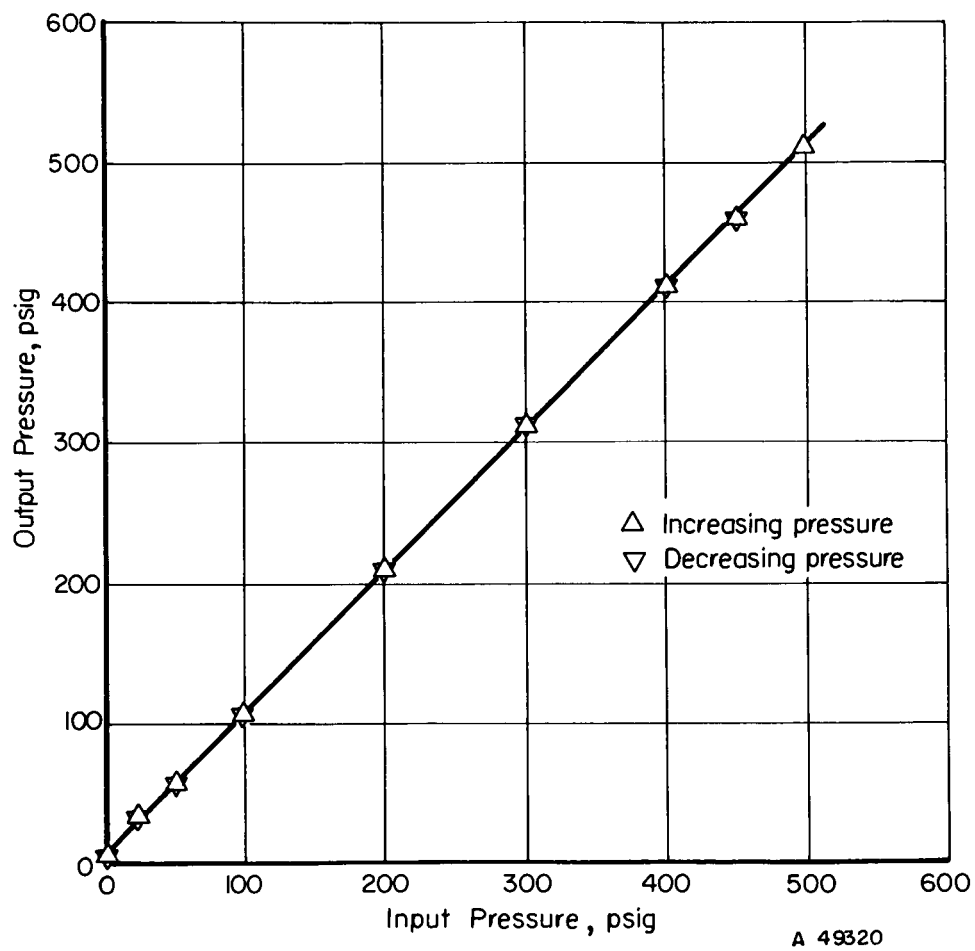
All stainless steel construction.

FIGURE 9. INPUT-OUTPUT RELATION OF THE DIAPHRAGM TRANSDUCER

analyses were planned to eventually attain an acceptable degree of confidence in the magnitude and variation of the time constant at different temperature levels.

The simplified analysis assumed that the probe had an infinite thermal conductivity (radial), would be heated by internal gamma heat generation and convection from the hot-gas stream, and would be cooled by radiative heat loss to the surrounding cold walls.

The number of variables encountered in a problem of this sort are conveniently handled in parametric form. Thus, fixing only three dimensionless parameters (under the assumptions of this simplified model) defines ν, the ratio of the probe temperature to the hot-gas temperature. These parameters are a time parameter, $\tau = t(h/\rho C_p L)^*$; a convection-radiation ratio, $A = h/\sigma_\epsilon T_f^3$; and an internal generation-convection ratio, $G = qL/hT_f$. Figure 10 is an overall illustration of these results with ν plotted versus τ and A and G varied parametrically. This corresponds to the case where at time zero the probe is at zero temperature and the reactor is instantly brought to power with the gas immediately at T_f, the internal-generation rate at q, and the convective coefficient at h. It is interesting to note that the case in which $G = 0$ and $A \longrightarrow \infty$ (convection only) is reasonably adequate. The range of variation of parameters of Figure 10 is representative of the intended application.

Examination of the tabulated values of ν_s (on Figure 10), the steady-state ratio of the probe temperature to the gas temperature shows that the value of the convection-radiation ratio, A, must be approximately 25 to make the probe temperature approach the gas temperature. Within the range of interest of this study, the generation-convection ratio has a smaller, though discernible, effect on ν_s.

The effect of radiative cooling is clarified with Figure 11. The smaller the value of the ordinate, $1-\nu$, the closer the probe temperature approaches the gas temperature. Curves with lower values of $1-\nu$ at any given value of τ (or time, since $h/\rho C_p L$ is constant) indicate cases of more rapid response. Considering first the cases with zero internal generation, it is seen that the higher the value of A (lower ratio of radiative cooling to convective heating at any given time) the more favorable the response is. It is clear from Figure 11 that a high convective coefficient is desirable, not only to reduce the actual time, t, required to reach a given value of τ, but also to overpower the radiative loss that would introduce error in the steady-state reading. The dashed curve, using a typical value of G for full-power operation and a somewhat optimistically high value of A, is an interesting coincidence; the response is more rapid than that of the convection only (no generation or radiation) case although the steady-state value of T is exactly T_f (shown in the tabulation, i.e., $1 - \nu_s = 0$).

Figure 12 is a further demonstration of the effect of internal heat generation q, on the response of the probe. In this plot it is apparent that as the ratio G is made larger by increasing q the time of response is materially shortened. Figure 12 is concerned with only one value of A, except for the convection-only comparison case. This value, 5, was estimated to be typical of the planned application. The typical application value for G was estimated to be 0.04. Thus it is seen that the anticipated response using these typical conditions is more rapid than the convection-only case initially but degenerates as radiation becomes important.

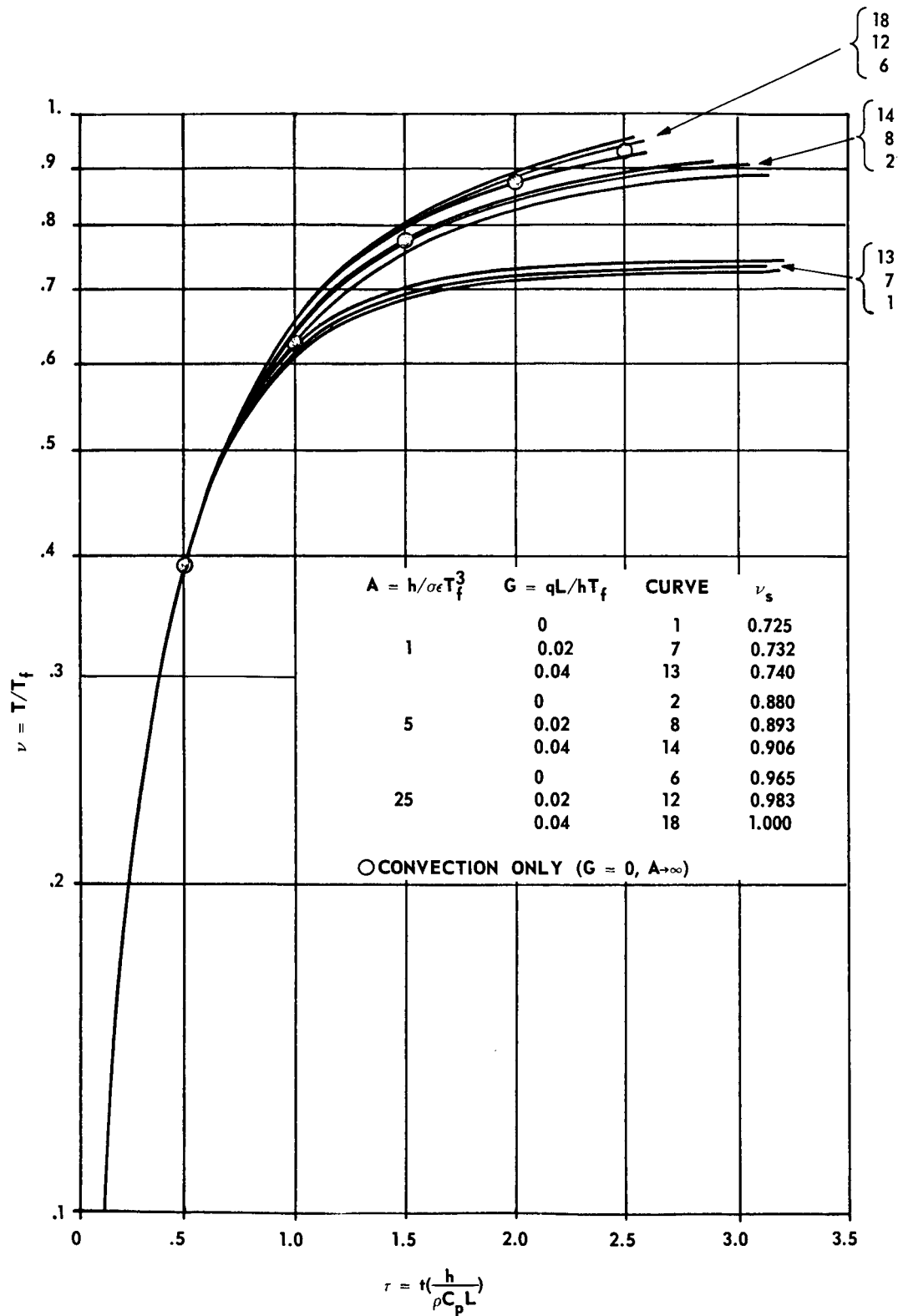*See Appendix for Nomenclature and derivation.

FIGURE 10.   RESPONSE OF PROBE ACCORDING TO SIMPLIFIED
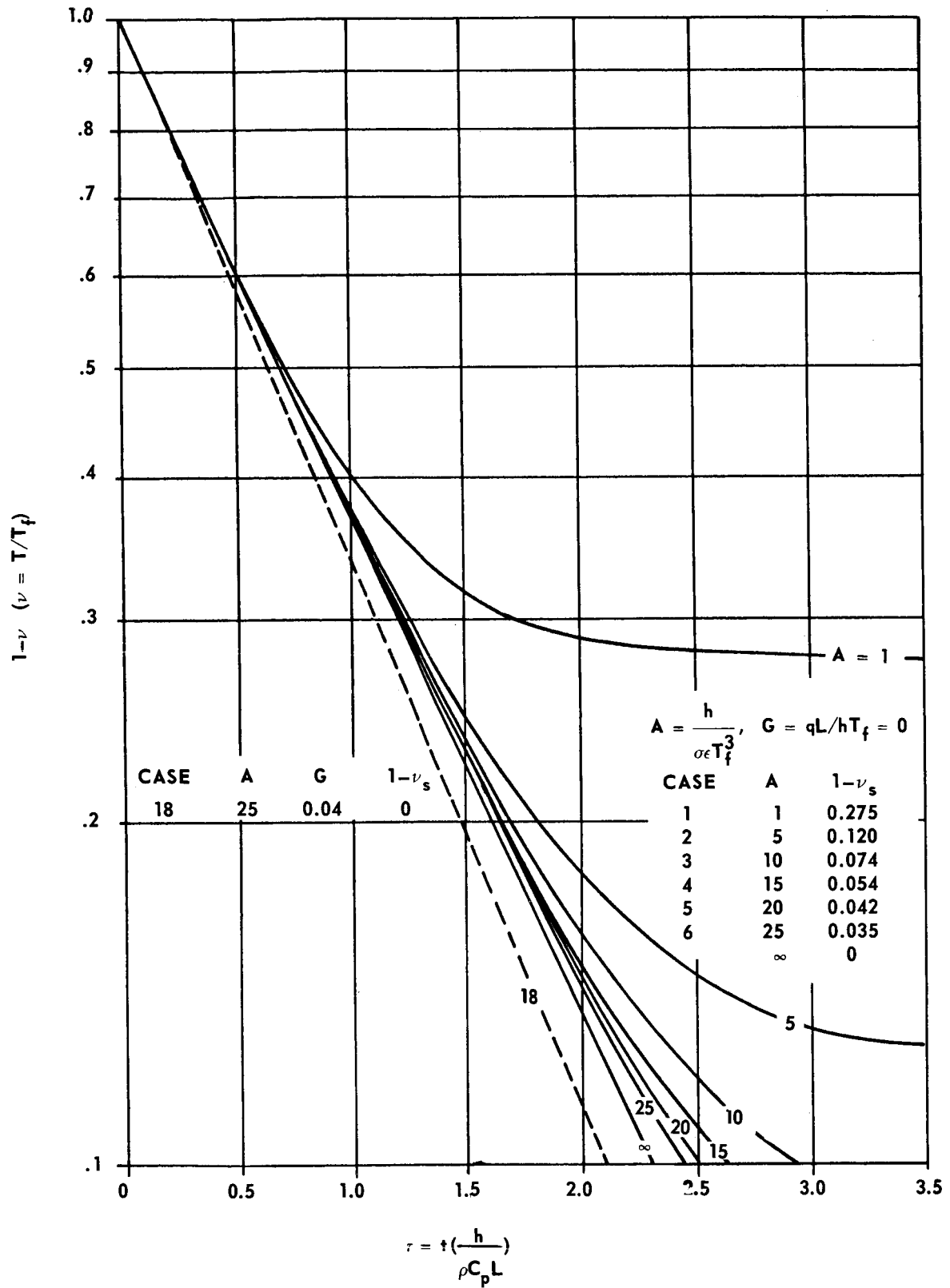TRANSIENT THEORY

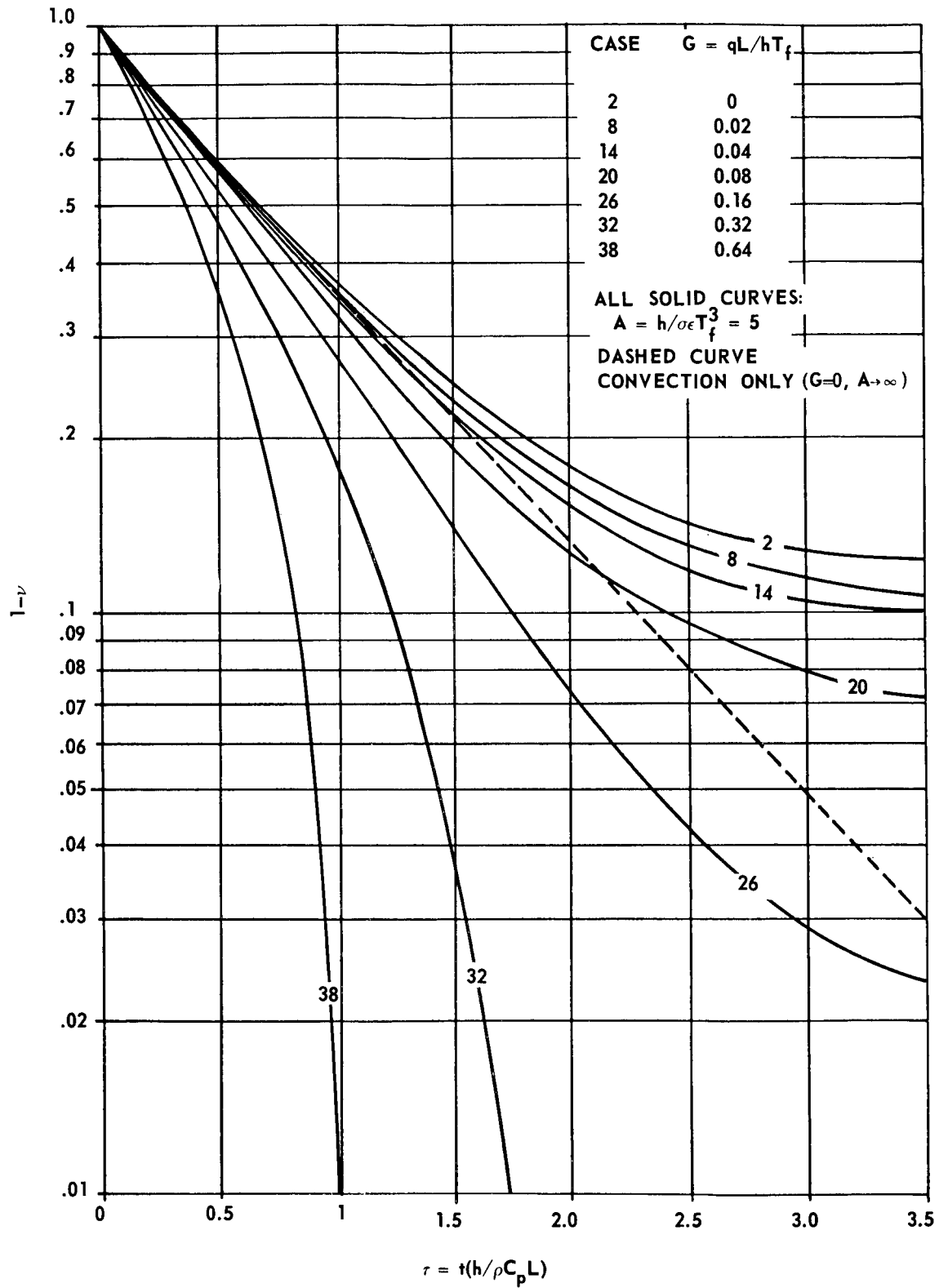FIGURE 11.   EFFECT OF RADIATION HEAT LOSS ON THE RESPONSE

FIGURE 12. EFFECT OF INTERNAL GENERATION ON THE RESPONSE

The steady-state solution[*] for the simplified model was obtained by equating dT/dt to zero. These results are shown in Figure 13 where the relative difference at steady state, $(T_s - T_f)/T_f$, is plotted versus A with G as a parameter. For the typical values of A and G of 5 and 0.04, $(T_s - T_f)/T_f$ is about -0.1, thus indicating that if T_f is 5000 R, T_s is about 4500 R.

Once the relative effects of radiative heat loss and internal heat generation on response were known, a relationship involving the time constant was established. The time constant is defined as the time required for the temperature difference between the gas temperature and the probe temperature to change by a factor of $1/e$. When the probe has only convective interchange with the environment, the time constant can be shown to be $\rho C_p L/h$. If radiative heat loss is introduced, the nonlinearity causes the effective time constant to be a function of temperature and whether or not the probe is heating or cooling. Figure 14 is a plot of the ratio of the effective time constant to $\rho C_p L/h$ versus the normalized probe temperature ν, for heating and cooling with the typical value of A = 5 while G = 0. The difference between heating and cooling is significant with the response on cooling being more rapid than on heating. However, as noted earlier, internal heat generation opposes radiative heat loss and would tend to lessen the spread between heating and cooling. The effects of q on the time constant ratio are apparent by comparing Figures 14 and 15. Comparison should be made between the curve marked "Heating With Radiative Loss Present", Figure 14, and the curve marked 0.04 in Figure 15. The latter contains the parameters A = 5 and G = 0.04 which were chosen earlier as typical values. The former contains A = 5, G = 0.

Examination of the typical curve (0.04) in Figure 15 reveals that a probe with a nominal time constant of 1/2 second would respond initially on heating with an effective time constant of about 0.48 second. When the probe temperature is about 0.4 times the gas temperature, i.e., about 2000 R for a gas temperature of 5000 R, the effective time constant is up to 1/2 second. It would gradually increase to about 0.75 second at 3500 R probe temperature and thereafter rise very rapidly because the steady-state temperature is less than the gas temperature.

In addition to the case of start-up from a very low probe temperature, cases of change in power at intermediate levels may be considered. For example, suppose steady state has been achieved with a gas temperature of 2930 R, a G ratio of 0.08, and an A ratio of 4. From Figure 13, it can be determined that the probe would be at about 2700 R. Let us assume that the gas temperature is suddenly raised to 4500 R, G changed to 0.04, and A to 5. Actually when T_f is increased, q and h will also be increased, so that changes in A and G with changes in operating conditions will not be drastic. Different values of A and G for the two operating conditions are used here to illustrate the generality of the curves. Immediately after the change in conditions, ν becomes 2700/4500 or 0.6. From Figure 15, it is seen that the immediate response of the probe with a nominal 1/2-second time constant now corresponds to a time constant of about 0.9 second. As the temperature is increased, the effective time constant increases, becoming infinite at steady state (about 4050 R), because the probe temperature is still less than the gas temperature.
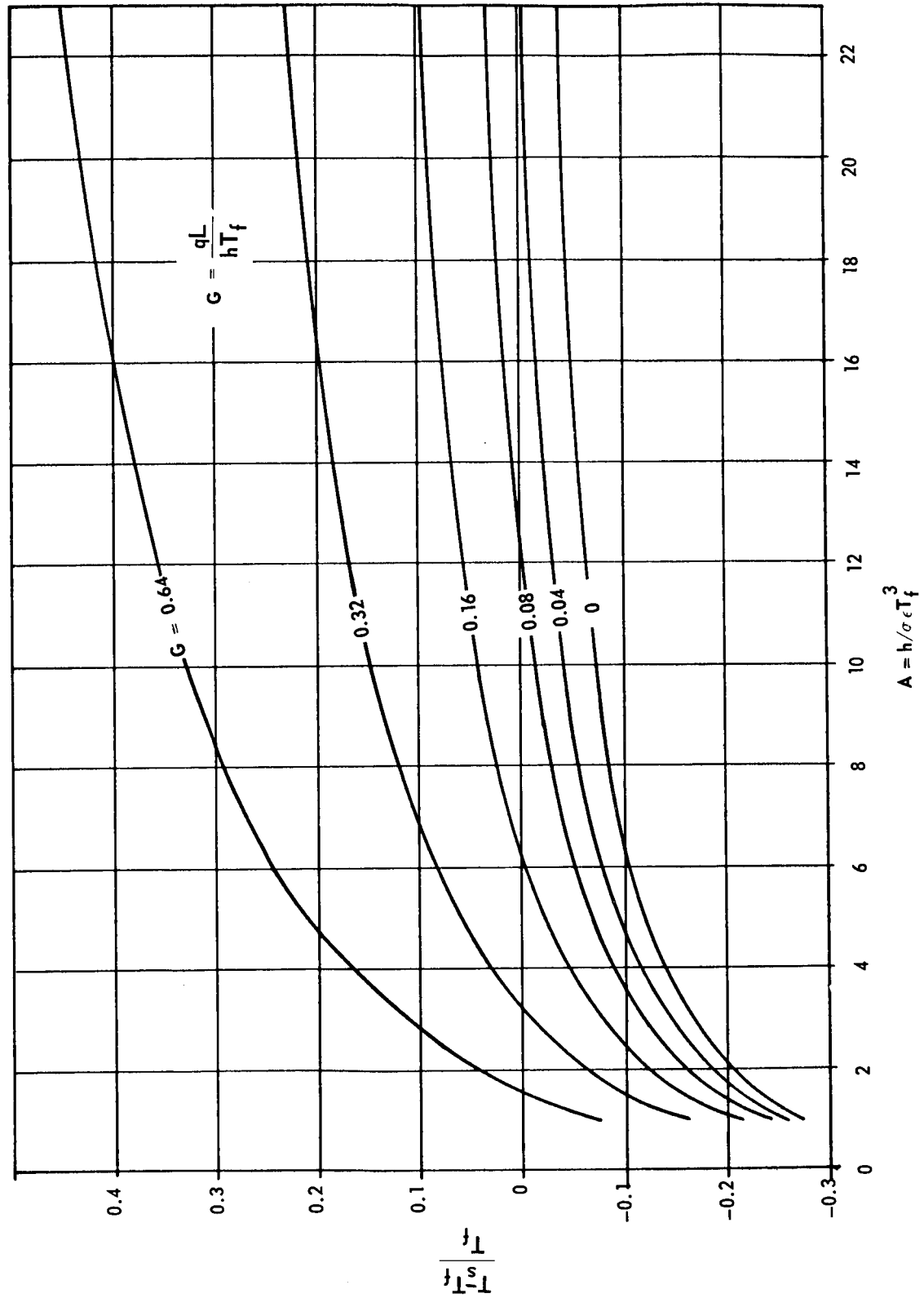
---

[*]See Appendix.

FIGURE 13. STEADY STATE TEMPERATURE RATIOS ACCORDING TO THE SIMPLIFIED TRANSIENT THEORY
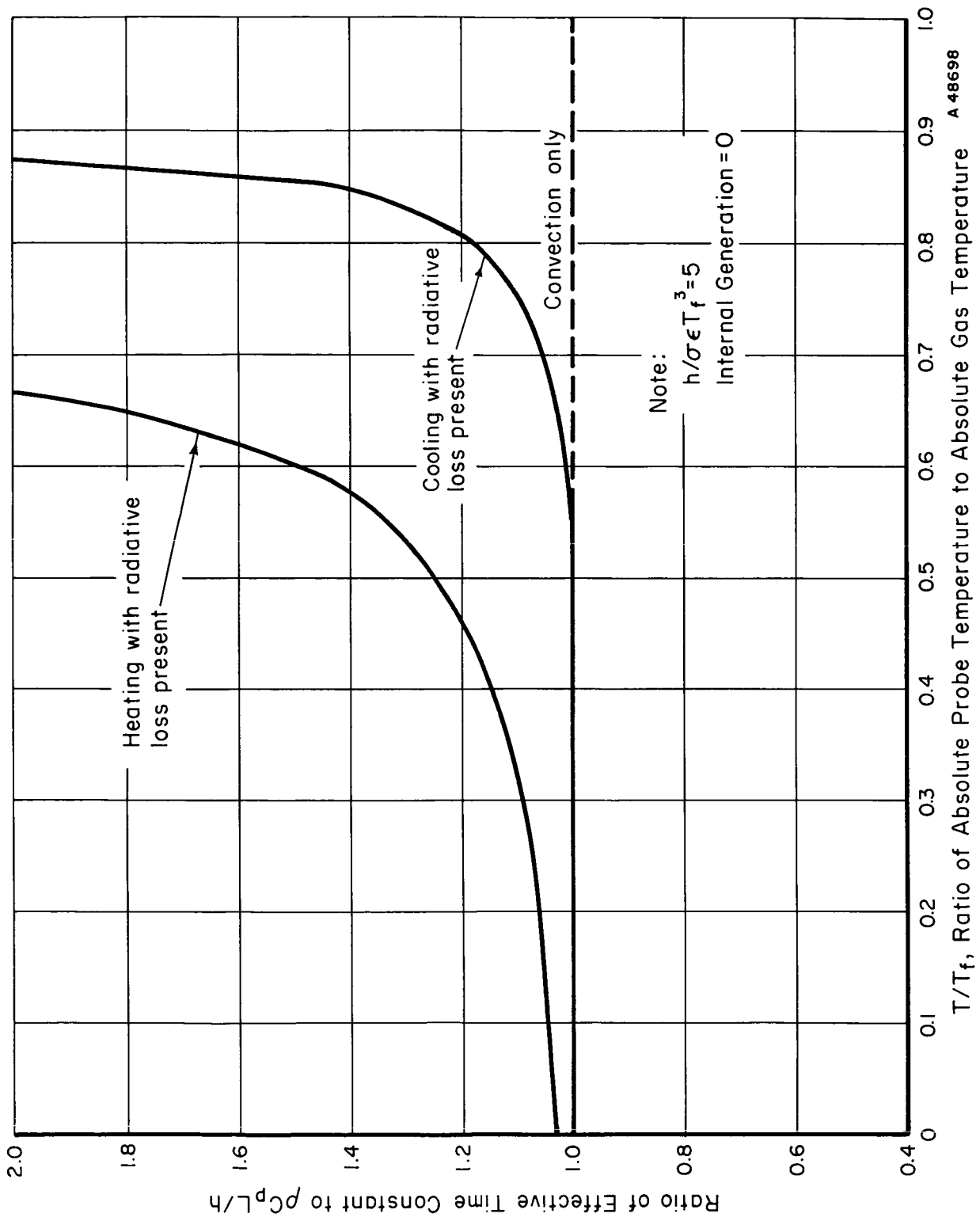
FIGURE 14. ILLUSTRATION OF THE DIFFERENCE IN RESPONSE ON HEATING OR COOLING WHEN RADIATIVE LOSS IS PRESENT
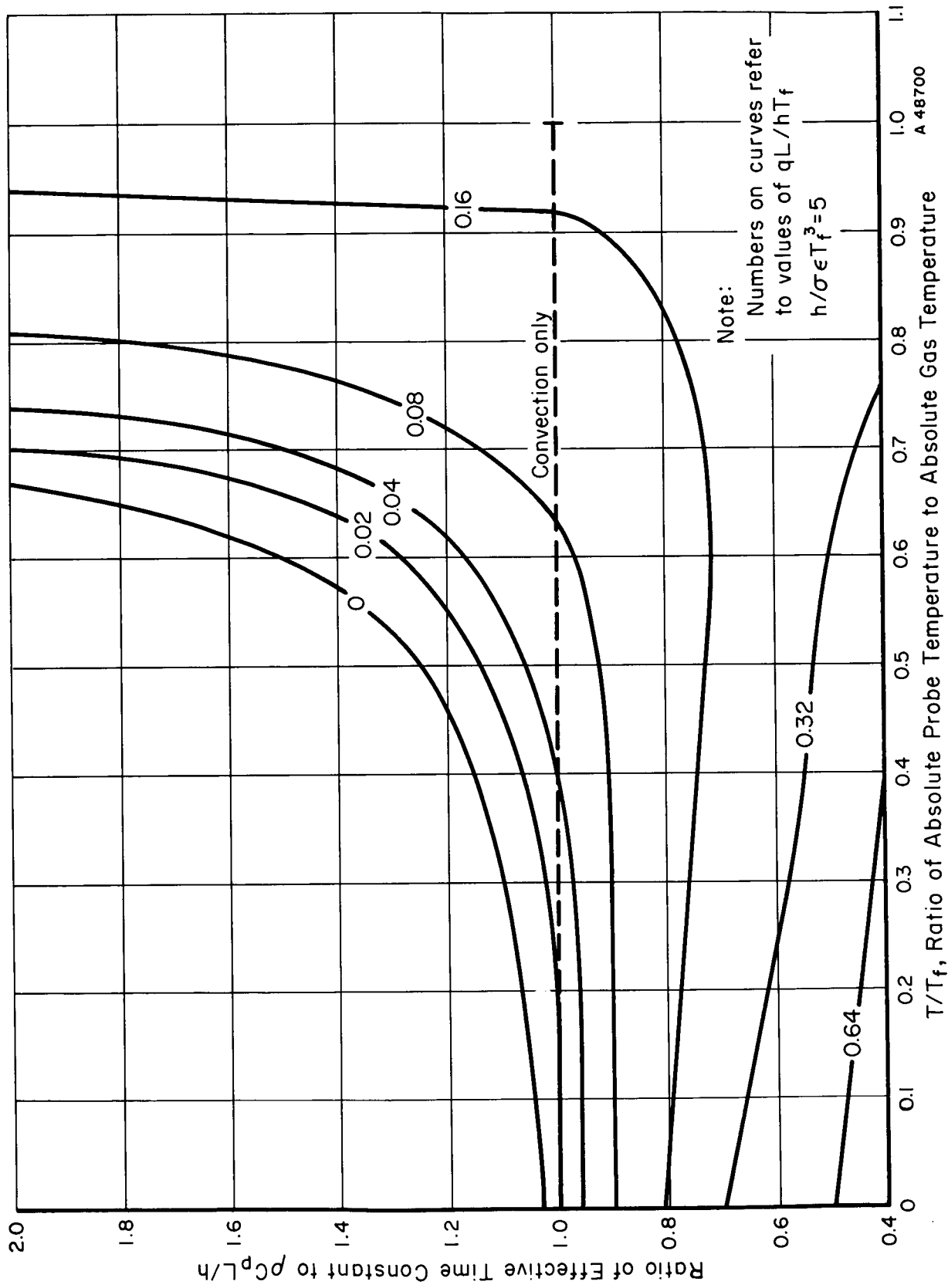
T/T$_f$, Ratio of Absolute Probe Temperature to Absolute Gas Temperature

FIGURE 15.   THE EFFECT OF INTERNAL HEAT GENERATION ON THE EFFECTIVE TIME
CONSTANT (NOMINAL RADIATIVE LOSS)

Conduction Losses Along the Length of the Probe

The importance of axial conduction as related to length of the probe has been considered using Battelle's two-dimensional steady-state heat-transfer program which will accept cylindrical geometry. The significant results of this study are shown in Figure 16. Table 6 illustrates the input data for the four cases. For surface temperatures less than the gas temperature, the convective input is greater than the internal heat generation, therefore temperatures decrease from the surface inward. Thus the maximum liquid-metal temperature at a given axial location is usually along the solid-liquid interface. These are the curves shown in Figure 16 for the four cases that were studied. These curves show that the axial heat loss may be minimized if the length of the probe is about four times its diameter. The calculated radial temperature differences (surface temperature minus center-line temperature) at the end cap-liquid metal interface for the four cases are 108, 36, 5, and -4 F for 1:1, 2:1, 3:1, and 4:1 length-to-diameter ratios, respectively. These values also indicate the advantage of a long probe.

The computer program did not permit radiative boundaries. Radiative loss was approximately accounted for by applying a convective coefficient on the cylindrical surface equivalent to radiative loss at a surface temperature of 4000 R, in addition to the normal convective heat input from the hot gas. This is obviously in significant error so that the curves of Figure 16 should be used only for comparison of lengths. The probable steady-state error in the temperature should not be obtained from this graph, but from Figure 13 instead. A hypothetical curve is sketched on Figure 16 illustrating qualitatively the proper effect of radiative loss on the temperature profile.

During this study it was also shown that the axial loss behavior of the probe is not greatly dependent on the wall thickness. If one considers the steady-heat conduction equation

$$k_i \left(\frac{\partial^2 T_i}{\partial r^2} + \frac{1}{r} \frac{\partial T_i}{\partial r} + \frac{\partial^2 T_i}{\partial z^2} \right) = q_i \quad .$$

The subscript, i, is either 1 or 2, referring to the solid metal container or the liquid metal. If the above equation is divided through by k_i, it is apparent that the system can be considered as one physical region with a "pseudo" thermal conductivity of 1, and a "pseudo" heat-generation rate of q_i/k_i. Inspection of Table 6 reveals that the ratio q_i/k_i is crudely the same for either material. This conclusion may also be drawn concerning a tungsten-bismuth system since the equality of q_i/k_i ratios is actually more closely approximated than for the tungsten-lead system.
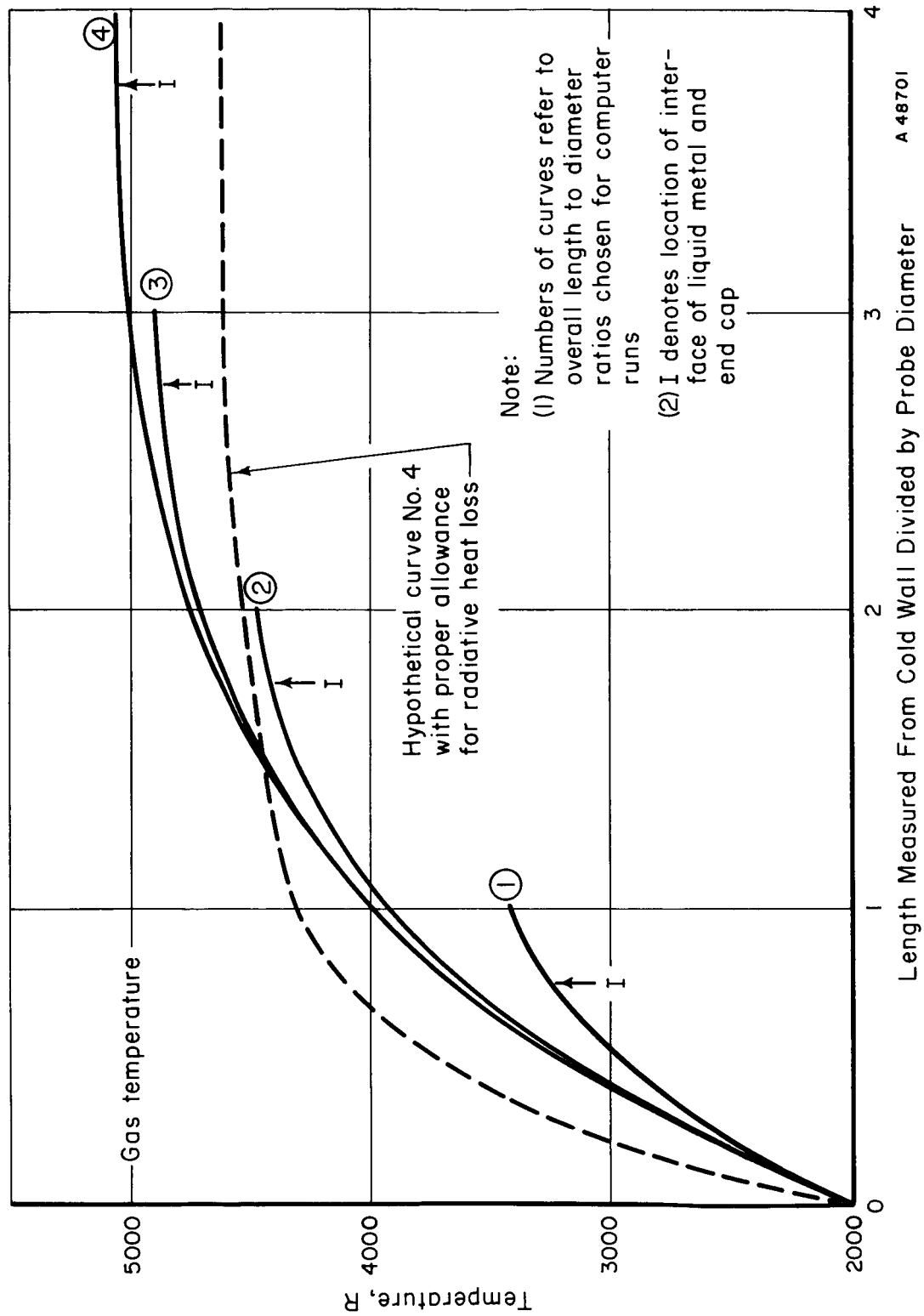
FIGURE 16. EFFECT OF PROBE LENGTH ON STEADY-STATE AXIAL TEMPERATURE PROFILE
ALONG SOLID METAL WALL

TABLE 6. INPUT PARAMETERS FOR AXIAL-HEAT-LOSS STUDY

Materials

Container	Tungsten
Liquid metal	Lead

Outside Diameter   1/4 inch

Wall Thickness   1/16 inch

End-Cap Thickness   1/16 inch

Thermal Conductivities

Lead	20 Btu/hr ft F
Tungsten	48 Btu/hr ft F

Gamma-Heat-Generation Rates

Lead $\qquad$ Tungsten $\qquad$ 10 watts/g $\begin{cases} 1.0 \times 10^7 \text{ Btu/hr ft}^3 \\ 1.7 \times 10^7 \text{ Btu/hr ft}^3 \end{cases}$

Cold-End Temperature   2000 R

Gas Temperature   5000 R

Emissivity of Tungsten   0.3

Convective Coefficient   1000 Btu/hr ft^2 F

APPENDIX

APPENDIX

Metallography

Photomicrographs showing the effects of high temperature on the compatibility of container materials and charging metals are presented in this appendix.
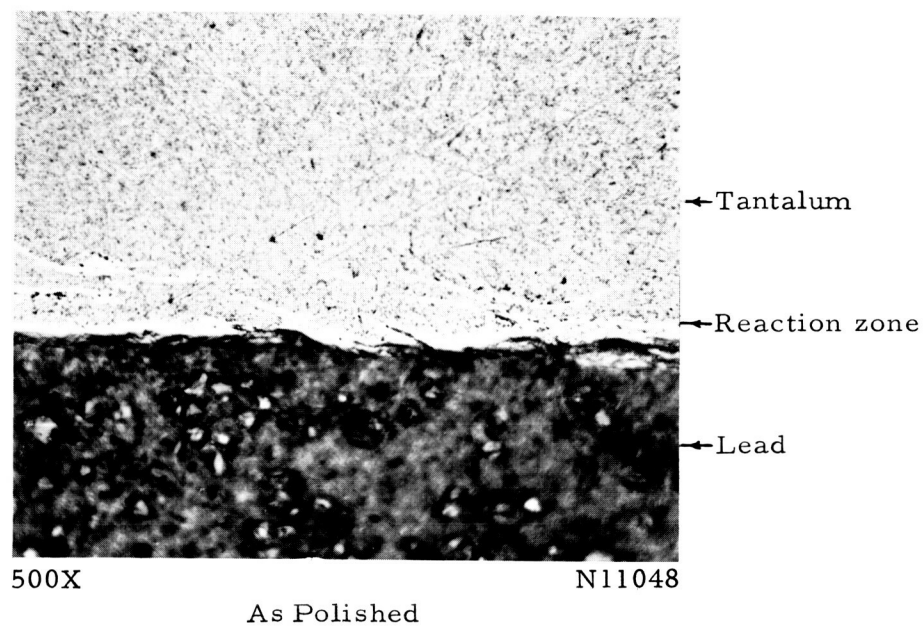
500X   N11048
As Polished

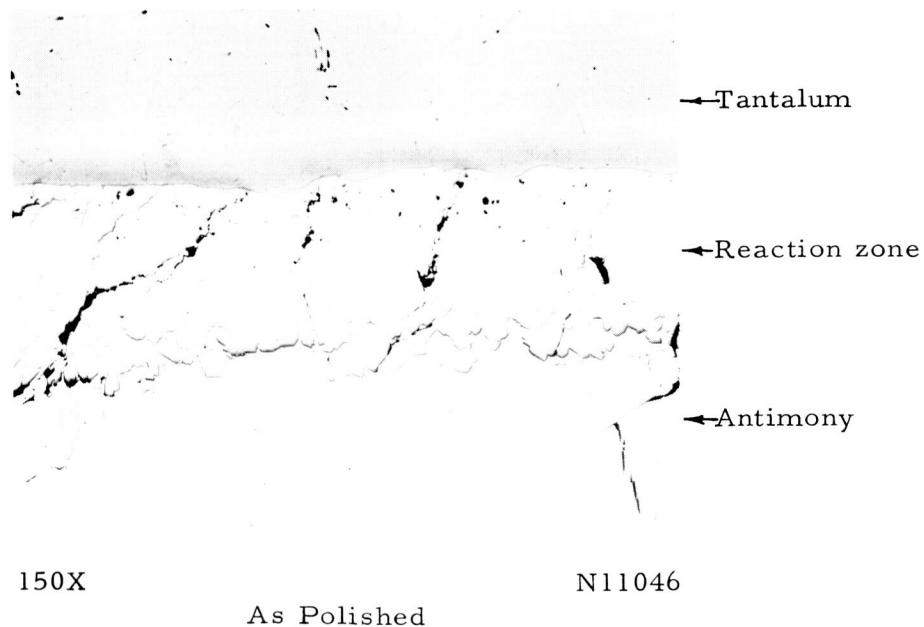FIGURE A-1.   COMPATIBILITY OF TANTALUM AND LEAD AT 2460 R FOR 1 HOUR

150X   N11046
As Polished

FIGURE A-2.   COMPATIBILITY OF TANTALUM AND ANTIMONY AT 2460 R
               FOR 1 HOUR

500X   N11047

As Polished
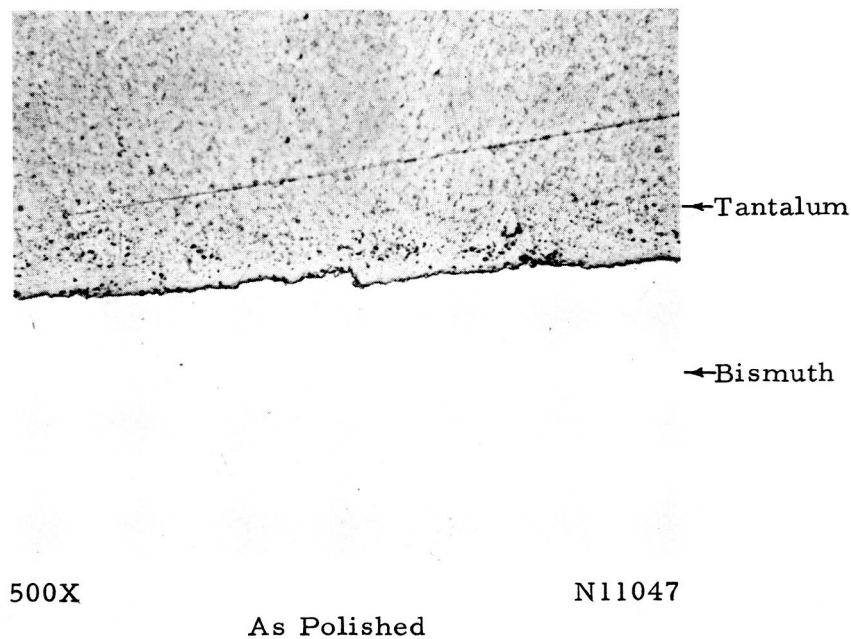
FIGURE A-3. COMPATIBILITY OF TANTALUM AND BISMUTH AT 2460 R FOR 1 HOUR

250X   N11494
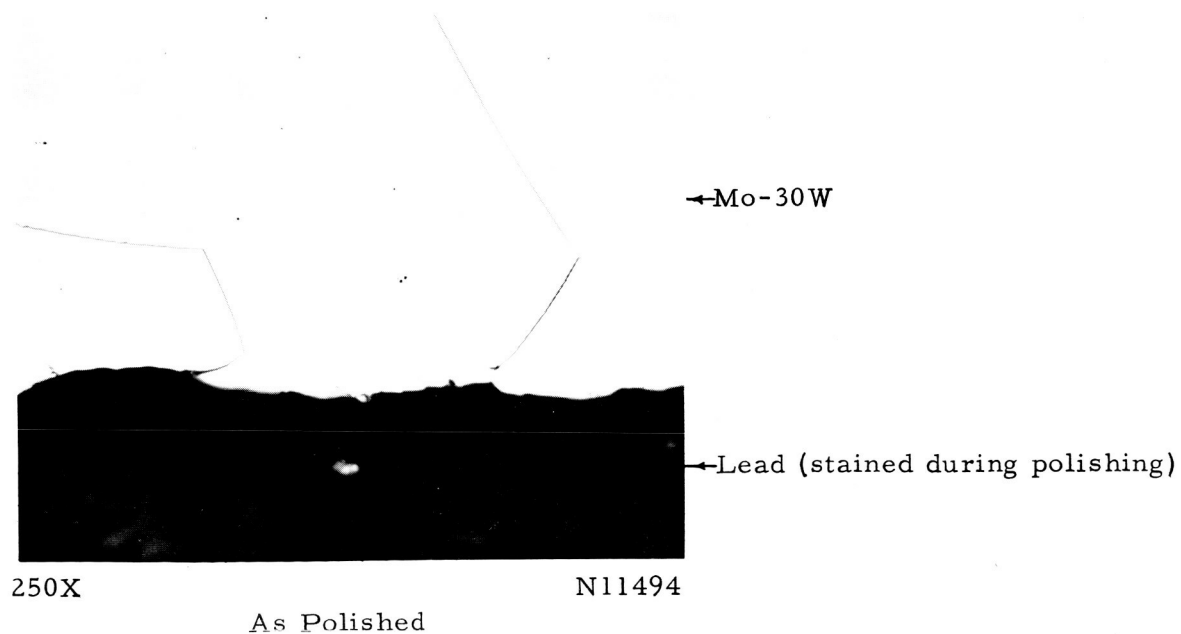
As Polished

FIGURE A-4. COMPATIBILITY OF Mo-30W AND LEAD AT 4000 R FOR 1 HOUR

←Bismuth

←Dark band is shrinkage space

←Mo-30W

250X   N11493
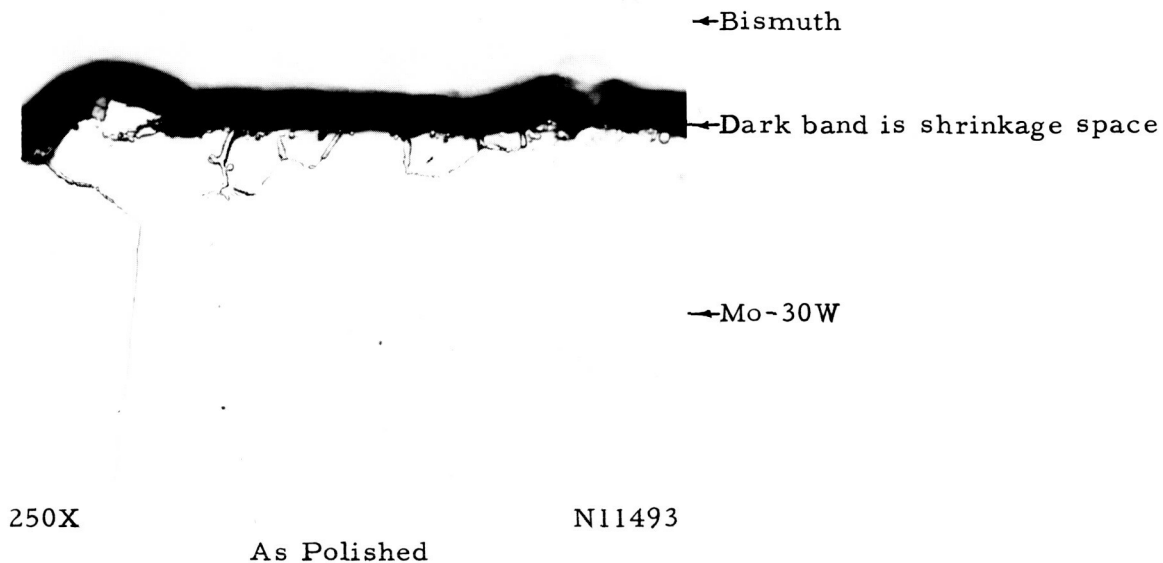
As Polished

FIGURE A-5.   COMPATIBILITY OF Mo-30W AND BISMUTH AT 4000 R FOR 1 HOUR

←Bismuth

←Shrinkage space
←Reaction zone

←Mo-30W

250X   N11492
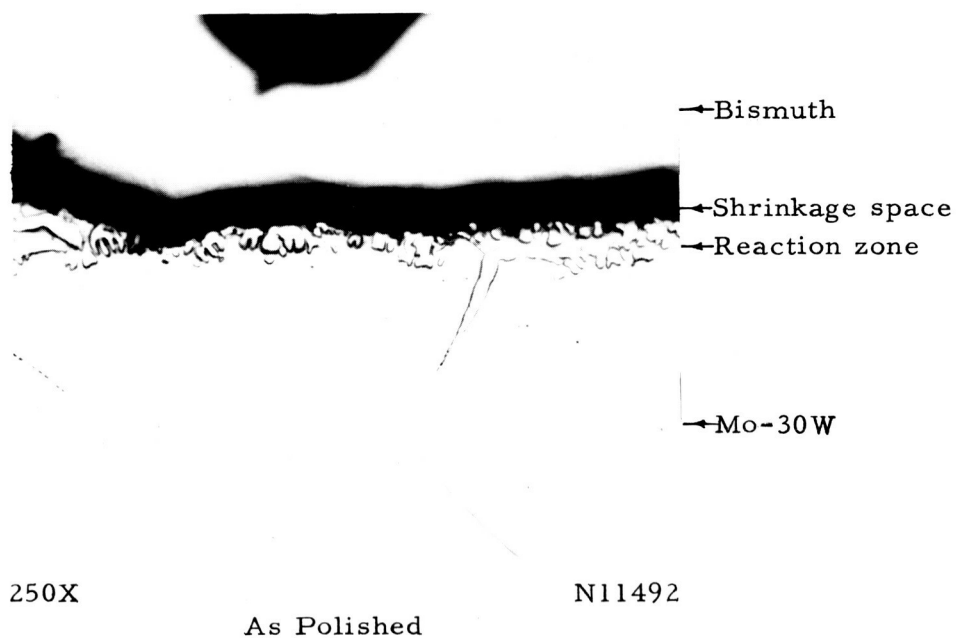
As Polished

FIGURE A-6.   COMPATIBILITY OF Mo-30W AND BISMUTH AT 4500 R FOR 1/2 HOUR

←Lead

←Reaction zone indicating solution of tungsten by lead

←Mo-30W

250X   N11495
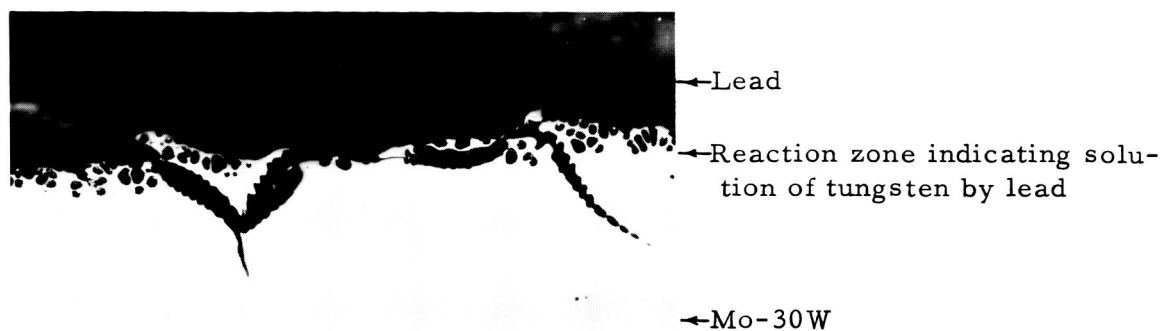
As Polished

FIGURE A-7.   COMPATIBILITY OF Mo-30W AND LEAD AT 4500 R
FOR 1 HOUR

←Tungsten

←Boundary between W and Bi

←Bismuth

500X   N11760
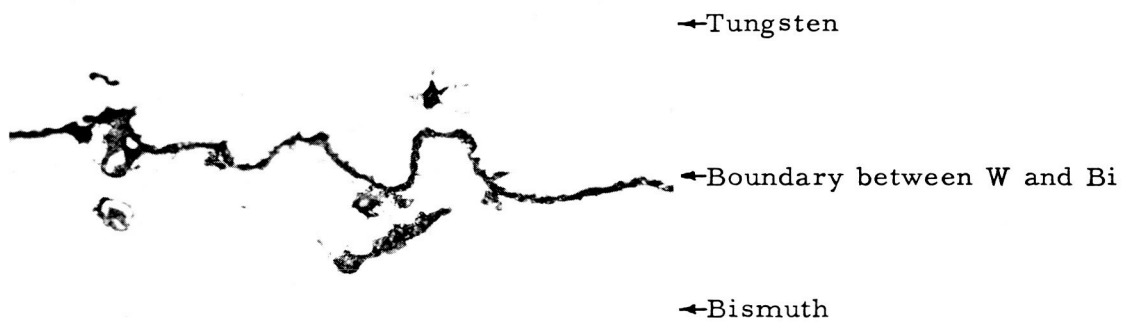
As Polished

FIGURE A-8.   COMPATIBILITY OF TUNGSTEN AND BISMUTH AT 4500 R
FOR 1 HOUR

←Bismuth

←Boundary between W and Bi

←Tungsten

500X   N11761
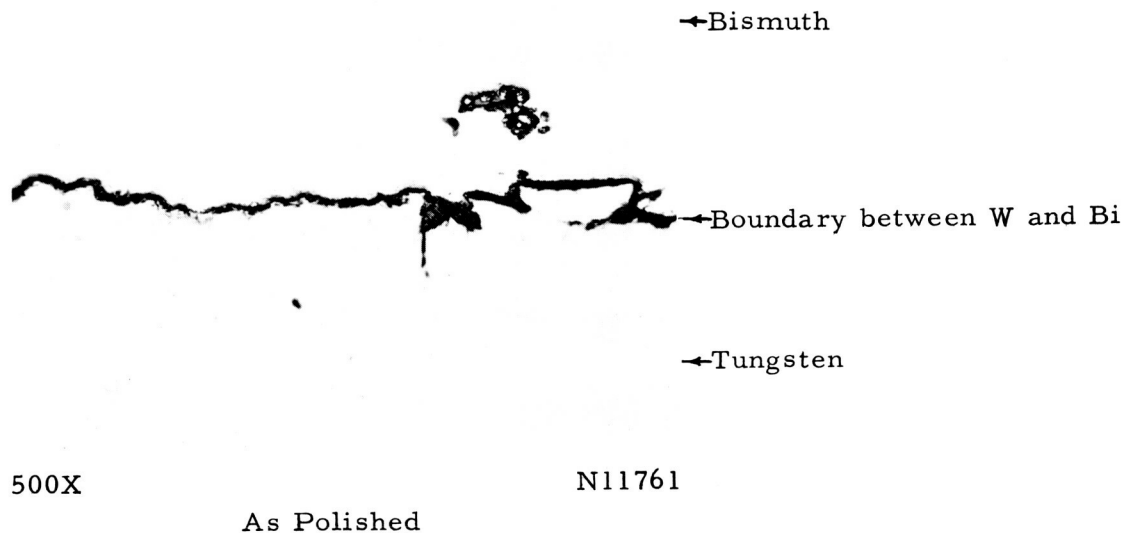
As Polished

FIGURE A-9.   COMPATIBILITY OF TUNGSTEN AND BISMUTH AT 5000 R
FOR 10 MINUTES

←Lead

←Reaction zone with tungsten
     fragments

←Tungsten

250X   N11941
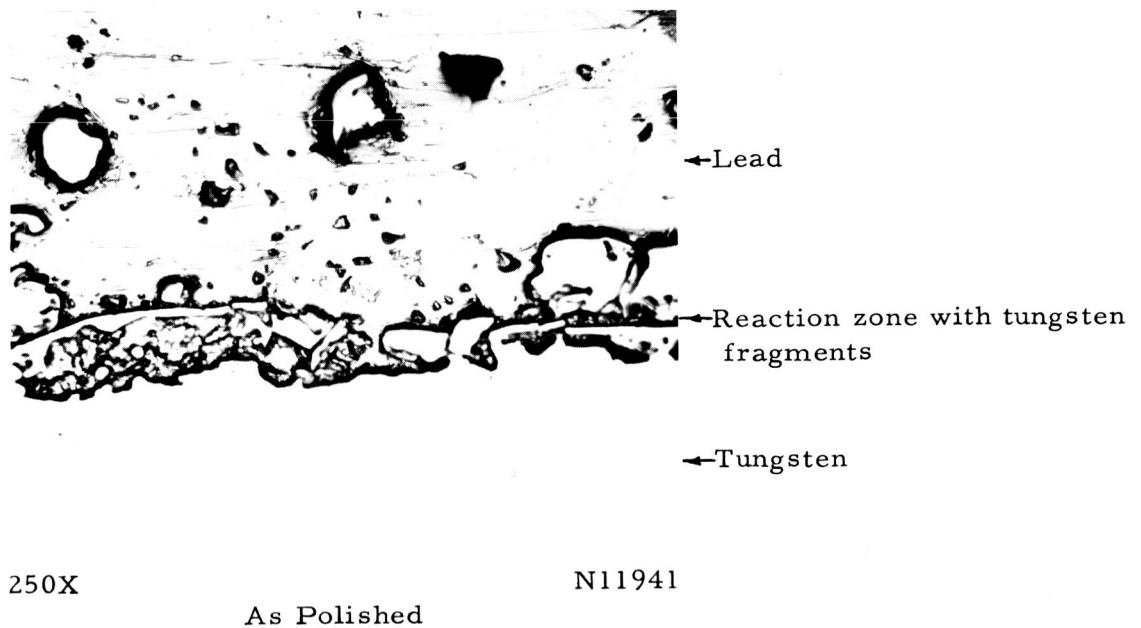
As Polished

FIGURE A-10.   COMPATIBILITY OF TUNGSTEN AND LEAD AT 4500 R
FOR 1 HOUR

→Lead

←Reaction zone with tungsten fragments

←Tungsten

250X   N11942
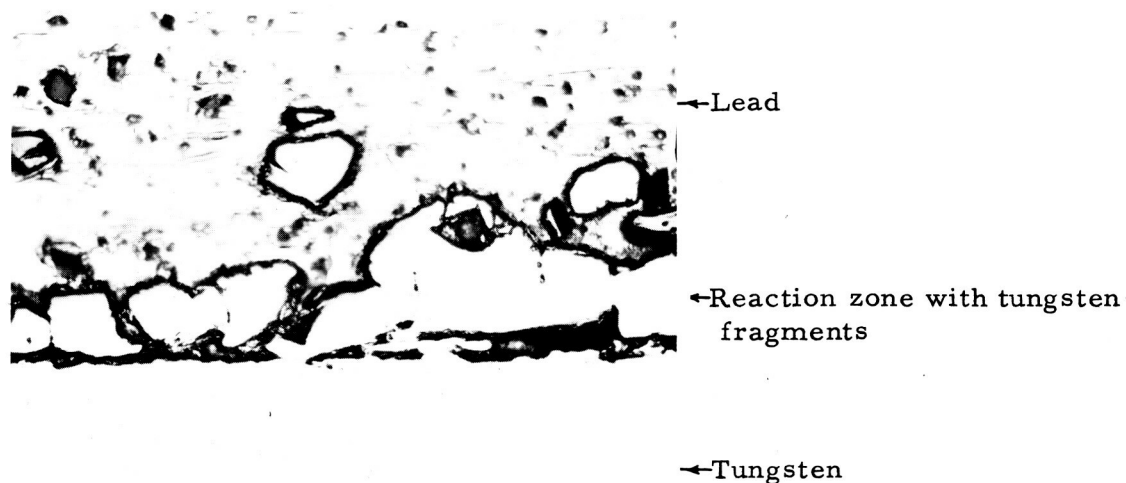
As Polished

FIGURE A-11.   COMPATIBILITY OF TUNGSTEN AND LEAD AT 4700 R FOR 25 MINUTES

←Antimony

←Black areas are voids along boundary

←Tungsten

250X   N11943
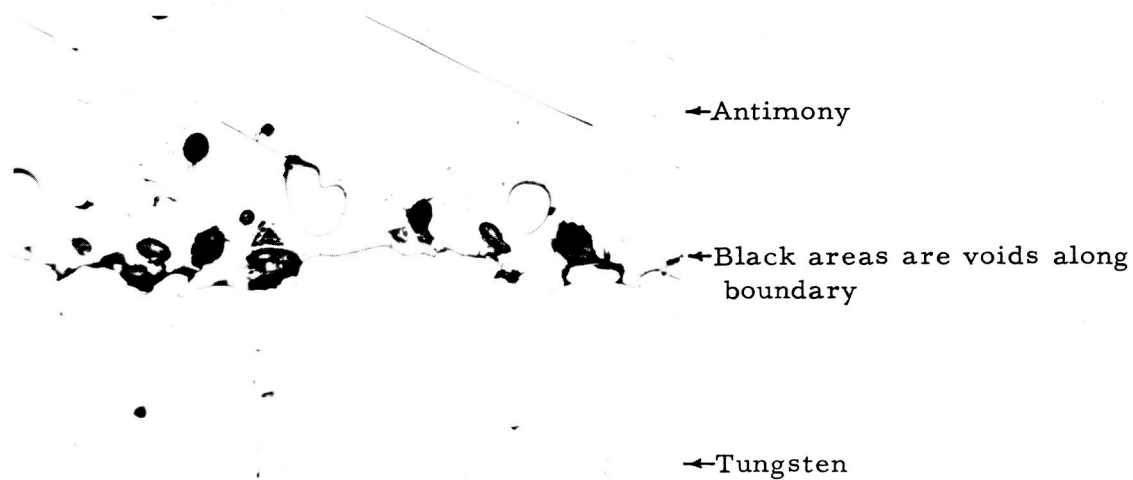
As Polished

FIGURE A-12.   COMPATIBILITY OF TUNGSTEN AND ANTIMONY AT 4500 R FOR 1 HOUR

←—Antimony

Black areas are voids

←—Boundary

←—Tungsten

250X   N11944

As Polished
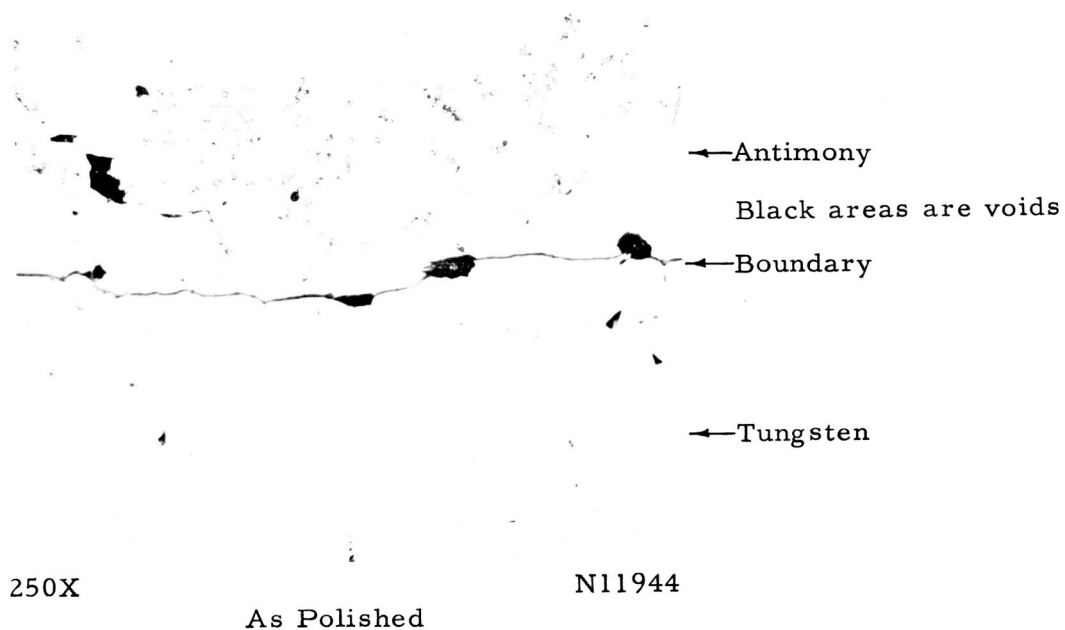
FIGURE A-13.   COMPATIBILITY OF TUNGSTEN AND ANTIMONY AT 5000 R
FOR 15 MINUTES
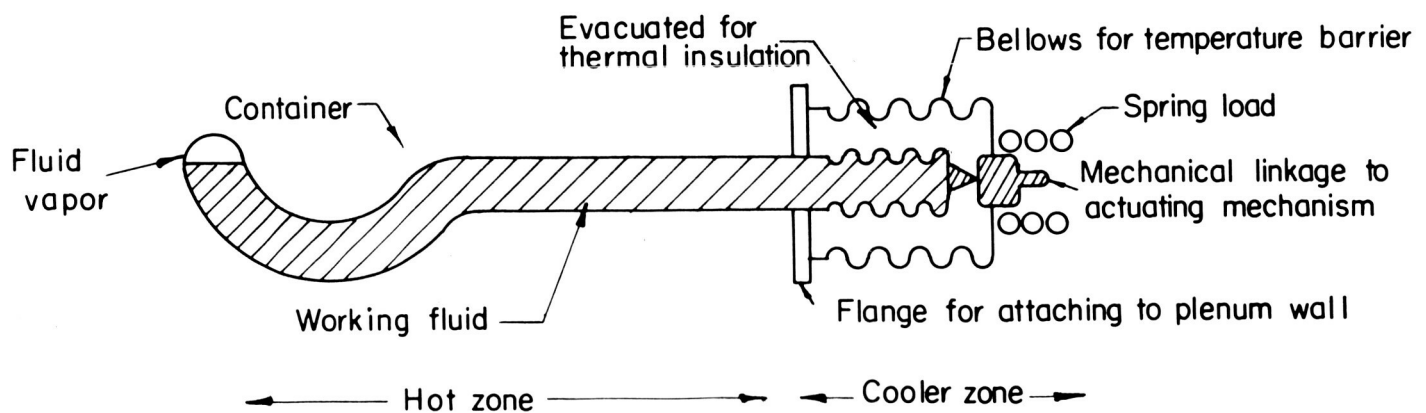
FIGURE A-14.   A POTENTIAL PROBE DESIGN FOR A HIGH-TEMPERATURE
SENSING DEVICE FOR CONVERTING VAPOR PRESSURE OF
A WORKING FLUID INTO A LINEAR MOTION

BATTELLE   MEMORIAL   INSTITUTE

250X   Light Murakami's Etch   14480

Black is mounting material

Reaction zone Mo-30W + Sb
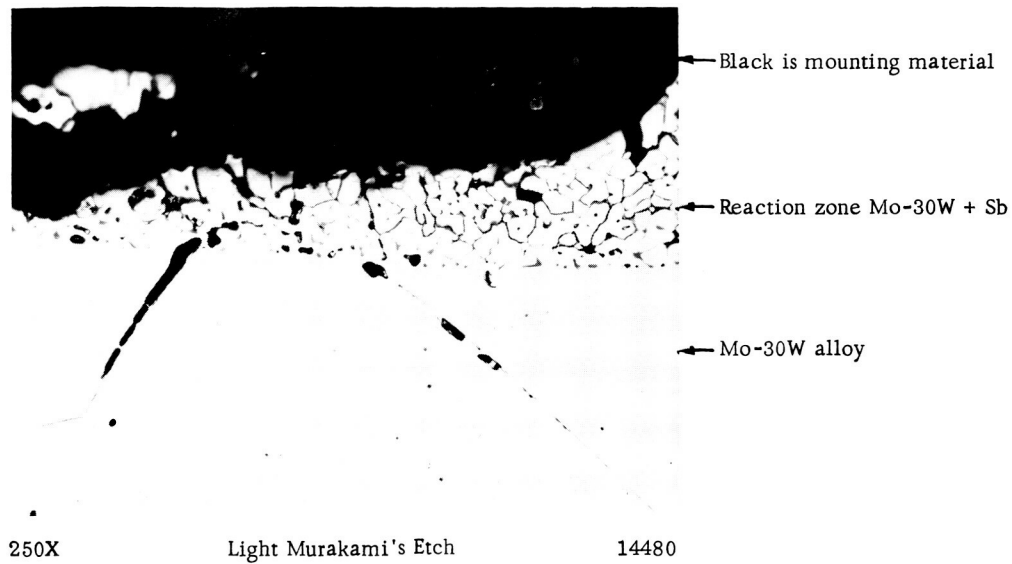
Mo-30W alloy

FIGURE A-15. COMPATIBILITY OF Mo-30W AND ANTIMONY AT
4500 R FOR 5 MINUTES

100X   Light Murakami's Etch   14481

Black is mounting material
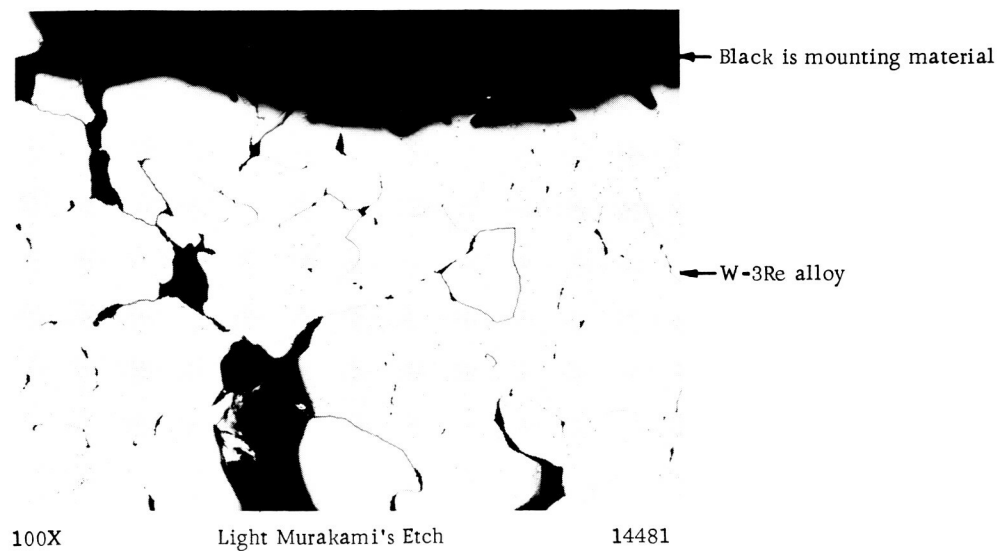
W-3Re alloy

FIGURE A-16. COMPATIBILITY OF W-3Re ALLOY AND BISMUTH AT 4500 R FOR
3 MINUTES, SHOWING SEVERE GRAIN-BOUNDARY ATTACK BY
BISMUTH, RESULTING IN RUPTURE OF SPECIMEN

Bismuth vaporized and is not present in failure.

←Antimony

←W-3Re alloy

White Phase is Sb. Penetration of grain boundaries has left dark voids.

250X   Light Murakami's Etch   14483
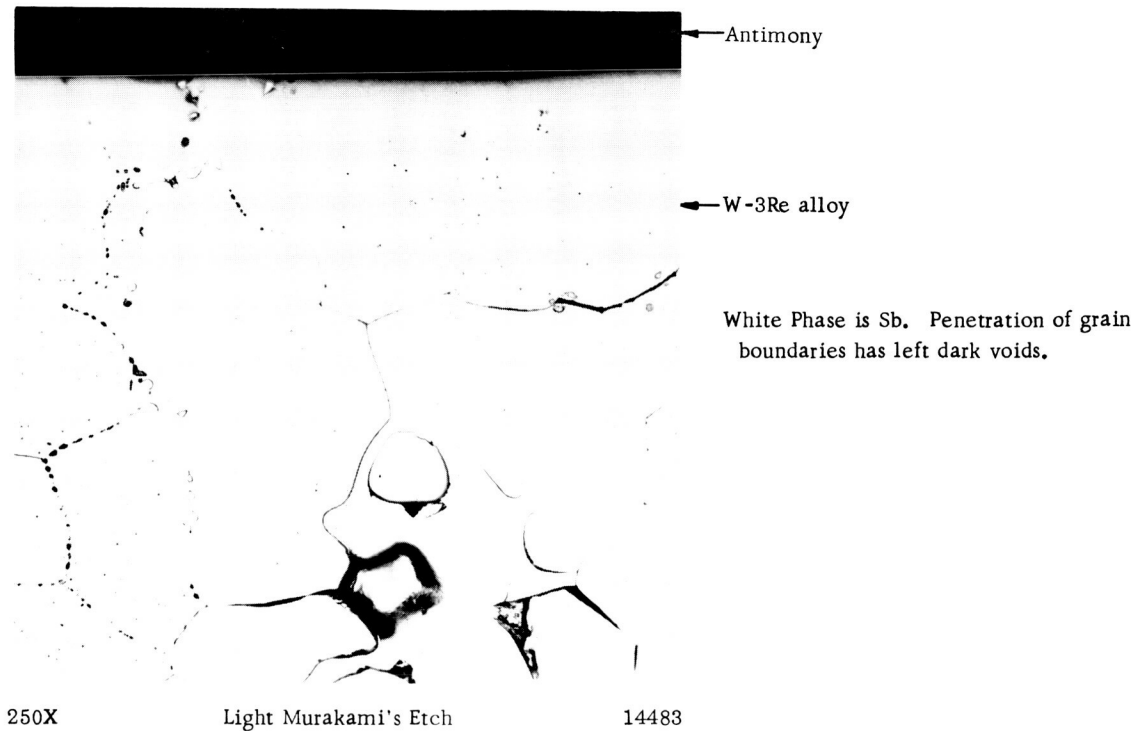
FIGURE A-17.   COMPATIBILITY OF W-3Re ALLOY AND ANTIMONY
                       AT 4500 R FOR 1 HOUR

Though no rupture occurred, grain-boundary penetration
was severe and rupture was imminent.

←Antimony

Mounting material in black areas

←W-3Re alloy

250X   Light Murakami's Etch   14484
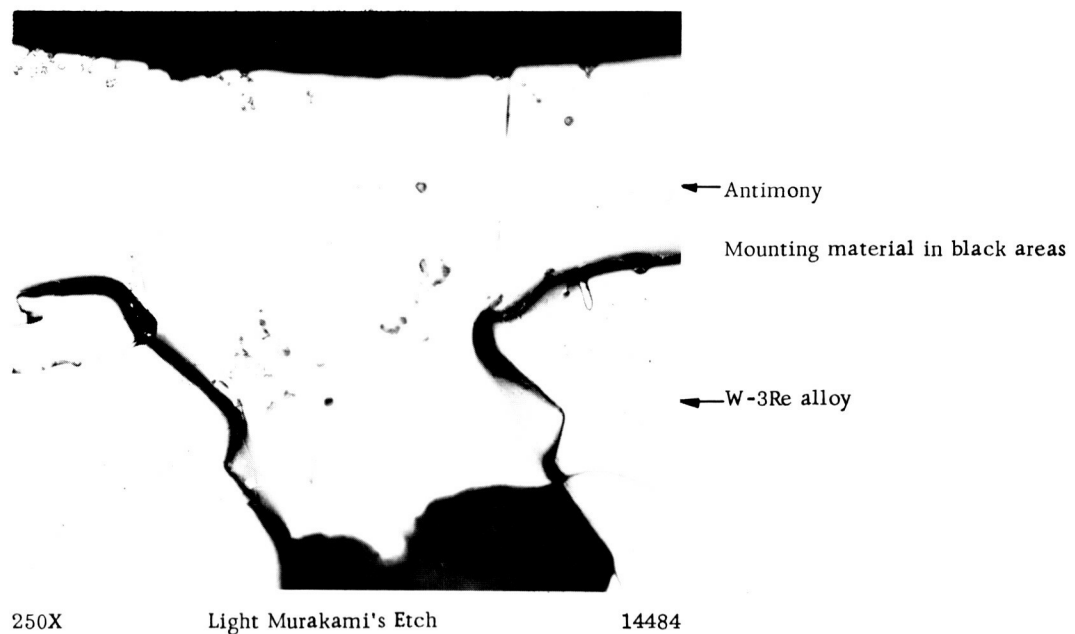
FIGURE A-18.   COMPATIBILITY OF W-3Re ALLOY AND
                       ANTIMONY AT 5000 R

Specimen ruptured in about 5 minutes.

250X   Light Murakami's Etch   14485
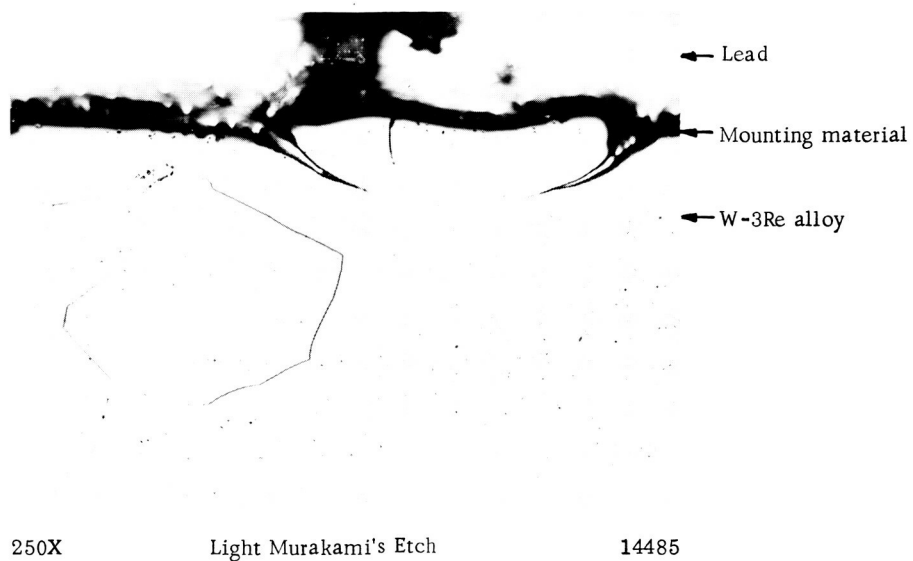
FIGURE A-19. COMPATIBILITY OF W-3Re ALLOY AND LEAD
              AT 4500 R FOR 1 HOUR

              Attack is slight. Depth of lead penetration
              about 0.002 inch.

250X   Light Murakami's Etch   14486
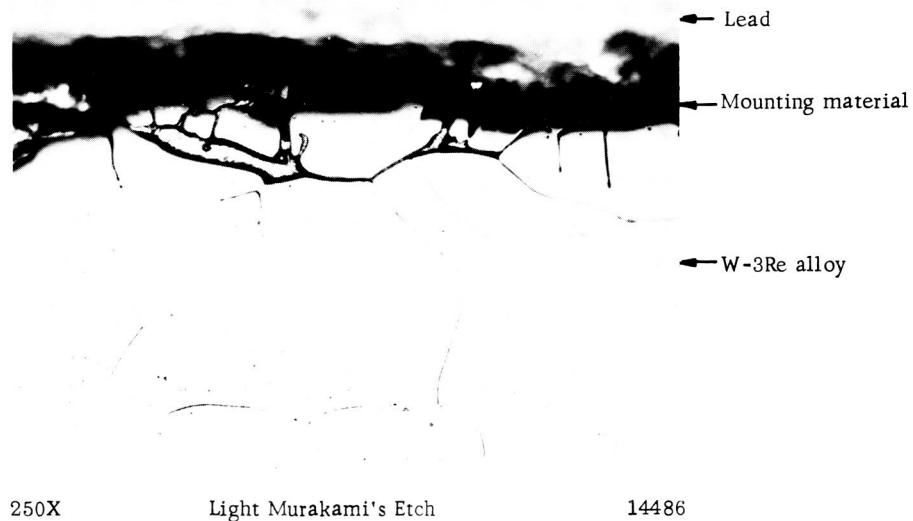
FIGURE A-20. COMPATIBILITY OF W-3Re ALLOY AND LEAD AT
              5000 R FOR 1 HOUR

              Grain-boundary attack stronger than at 4500 R, but
              maximum penetration only about 0.0025 inch.

250X   Murakami's Etch   15085
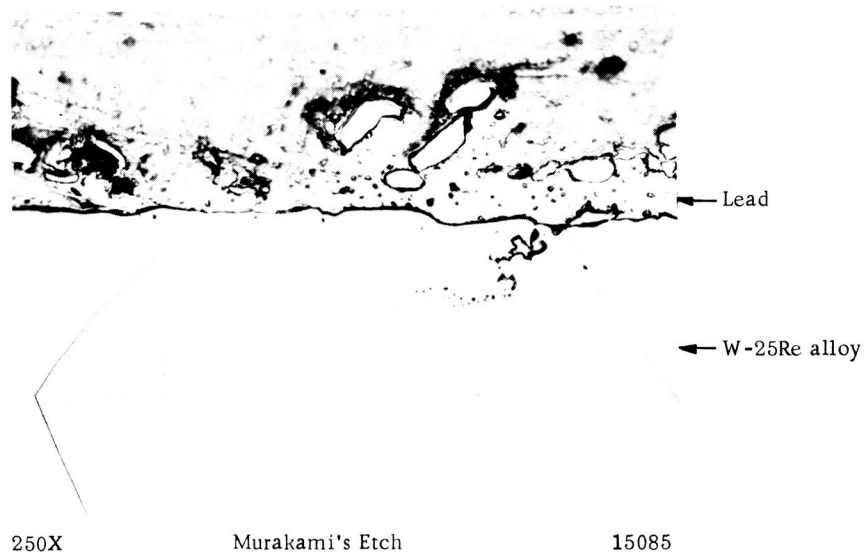
FIGURE A-21.   COMPATIBILITY OF W-25Re ALLOY AND LEAD AT
4500 R FOR 1 HOUR

Attack is considered minor. Angular particles are
believed to be remnants from the rough base.

250X   Murakami's Etch   15086
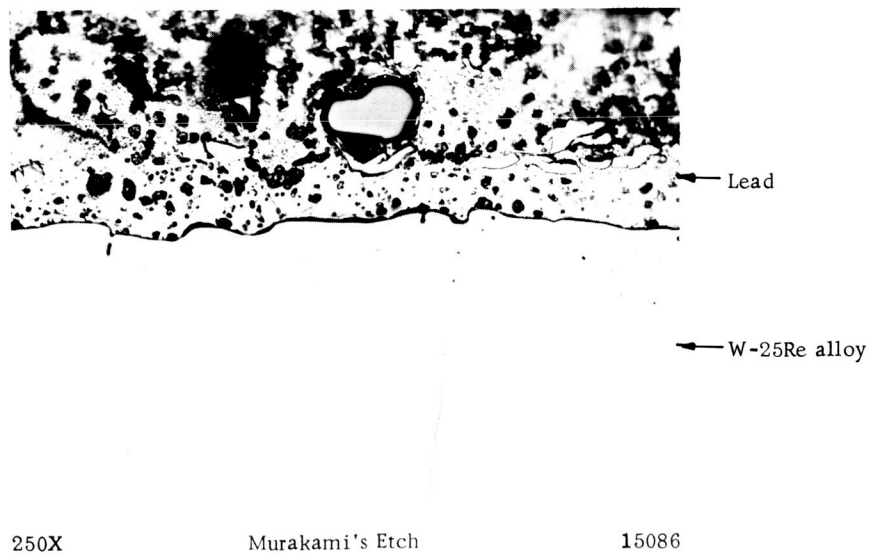
FIGURE A-22.   COMPATIBILITY OF W-25Re ALLOY AND LEAD
AT 5000 R FOR 1 HOUR

Lead shows porosity in this area and a few frag-
ments of W-Re alloy.

| 250X | Murakami's Etch | 15087 |
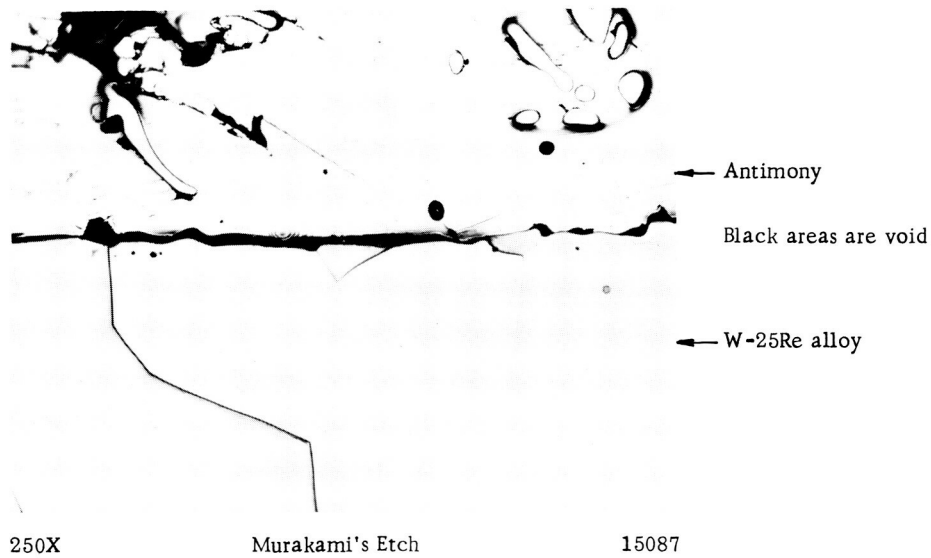
FIGURE A-23. COMPATIBILITY OF W-25Re ALLOY AND ANTIMONY AT 4500 R FOR 1 HOUR

Attack by antimony appears minor.

| 250X | Murakami's Etch | 15088 |
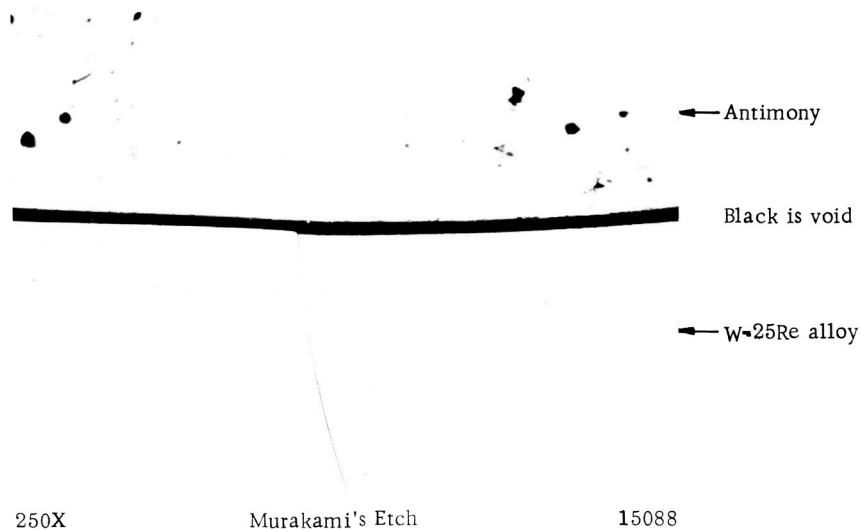
FIGURE A-24. COMPATIBILITY OF W-25Re ALLOY AND ANTIMONY AT 5000 R FOR 1 HOUR

Reaction between the two metals appears absent. However, the sample expanded about 2.4 per cent in diameter owing to creep.

← Bismuth

← Polishing undercut

← W-25Re alloy

250X   Murakami's Etch   15089
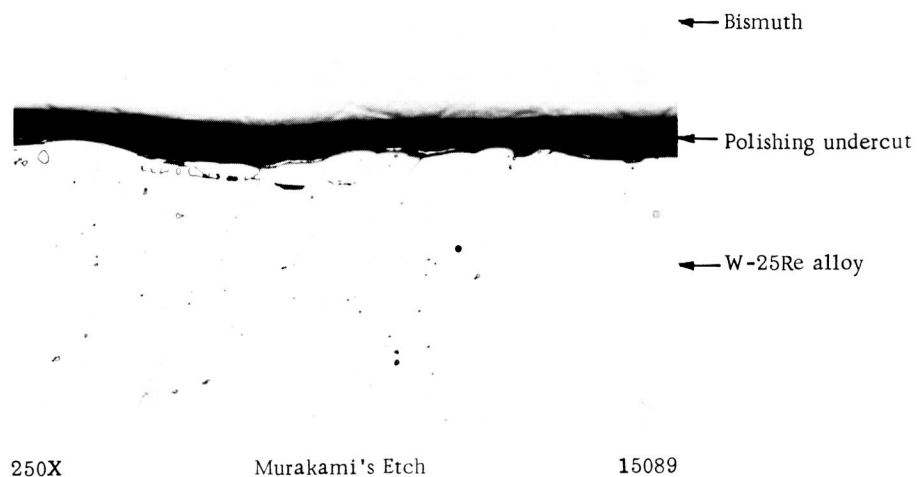
FIGURE A-25. COMPATIBILITY OF W-25Re ALLOY AND
BISMUTH AT 4500 R FOR 1 HOUR

Shows only very slight attack.

← Mounting material

← W-25Re alloy

250X   Murakami's Etch   15090
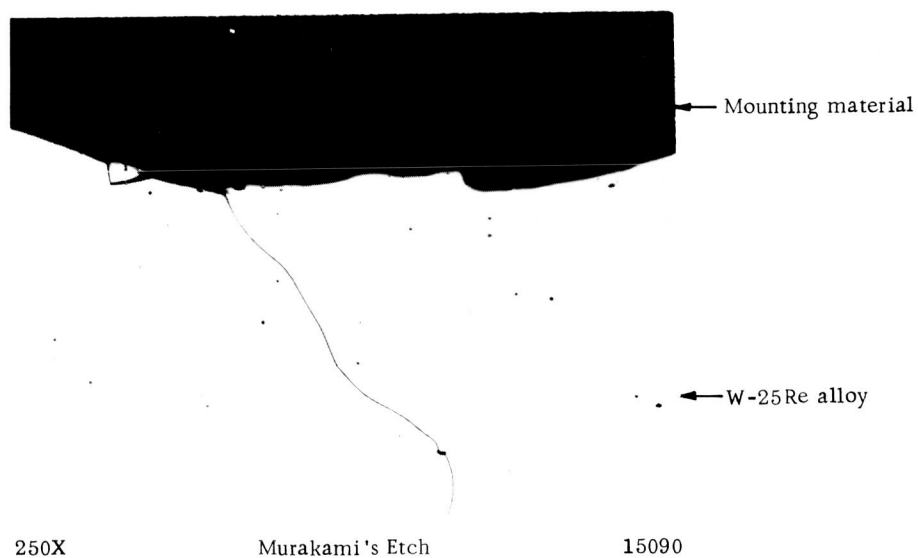
FIGURE A-26. COMPATIBILITY OF W-25Re ALLOY AND
BISMUTH AT 5000 R FOR 50 MINUTES

Sample burst in creep and bismuth was
vaporized. Bismuth is not believed to
have attacked the W-25 Re alloy.

250X   5% Chromic Etch   15091
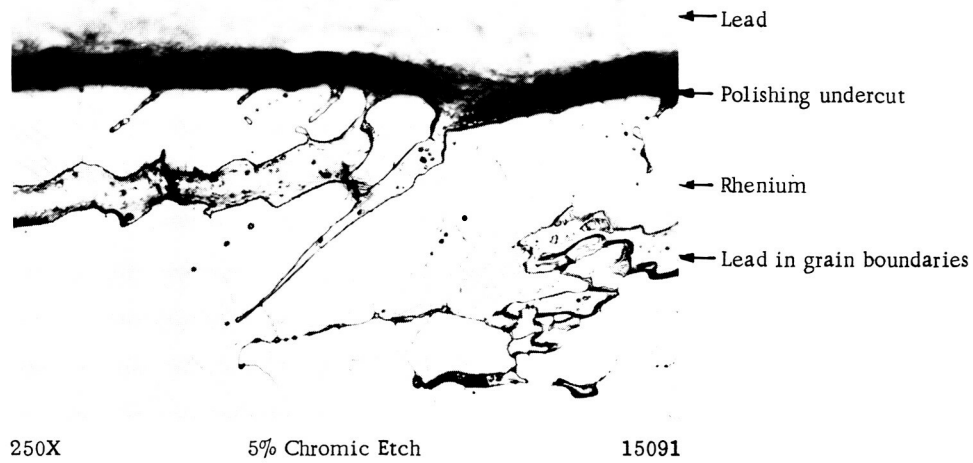
FIGURE A-27. COMPATIBILITY OF RHENIUM AND LEAD AT
5000 R FOR 1 HOUR

Penetration of grain boundaries by lead is
evident though sample did not fail.

250X   5% Chromic Etch   15092
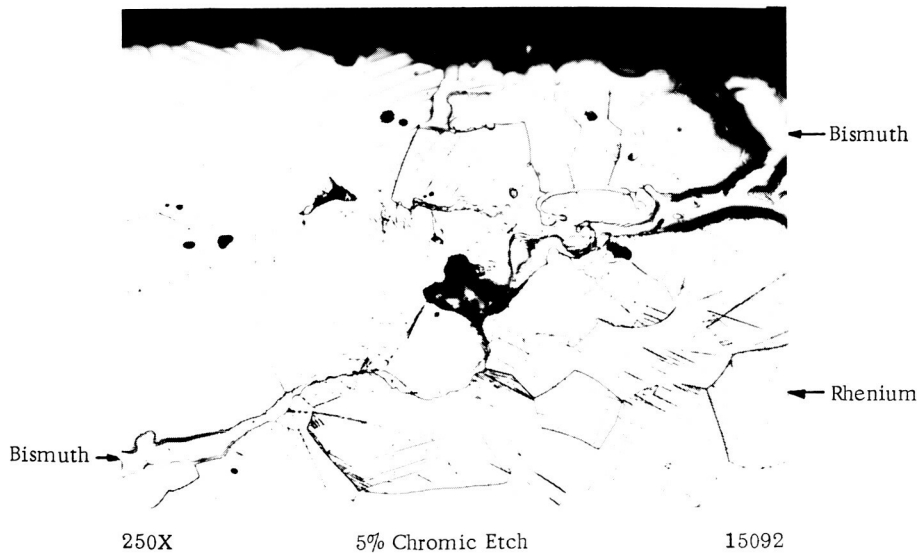
FIGURE A-28. COMPATIBILITY OF RHENIUM AND BISMUTH AT
5000 R FOR 1 HOUR

Grain-boundary attack is severe but failure did not
occur.

Materials From Which Specimens for Evaluation as Sensor Probes Were Made

FIGURE A-29. TUNGSTEN-
3 PER CENT RHENIUM ALLOY;
AS-RECEIVED

1000X   Murakami's Etch   N20045

FIGURE A-30. UNALLOYED
TUNGSTEN; AS-RECEIVED

1000X   Murakami's Etch   N20046
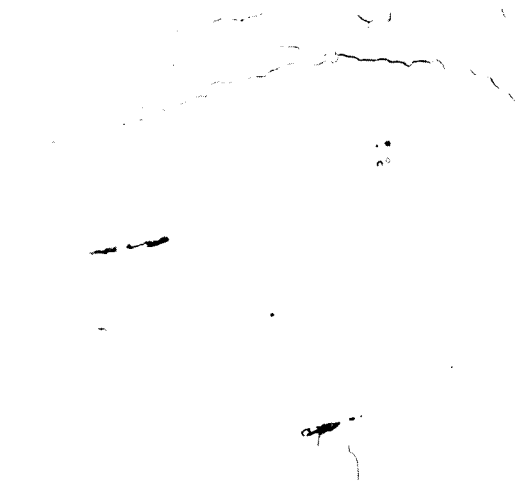
FIGURE A-31. TUNGSTEN-
25 PER CENT RHENIUM

1000X   Murakami's Etch   N20043

B A T T E L L E   M E M O R I A L   I N S T I T U T E

Creep Criteria

Long-time creep can be expressed mathematically as

$$\epsilon = kt\left(\frac{S}{S_o}\right)^n ,$$

where

ϵ = creep, in./in.

k = material parameter, $\dfrac{\text{in./in.}}{\text{day}}$

t = elapsed time, day
(the unit of time may be other than a day if convenient)

S = imposed stress due to loading, psi

S_o = normalizing stress, psi
(this stress is required to give a nondimensional relation and
allow extrapolation from experimental data)

n = material parameter, nondimensional, experimentally determined

For an estimate of allowable stresses, this relation may be used to establish pertinent ratios:

$$1 = \frac{\epsilon = kt_1\left(\dfrac{S_1}{S_o}\right)^n}{\epsilon = kt_2\left(\dfrac{S_2}{S_o}\right)^n} = \frac{t_1 S_1^{\,n}}{t_2 S_2^{\,n}} ,$$

or

$$(t_2/t_1) = (S_1/S_2)^n .$$

Extended use will be defined as 100 hours, thus making the ratio, (t_2/t_1), equal to 100. Then,

$$(S_1/S_2) = (t_2/t_1)^{1/n} = \sqrt[n]{100} .$$

Values of n usually range upward from $n = 4$, so

$$(S_1/S_2) = \sqrt[4]{100} = 3.17.$$

Then if the 2 per cent creep is to be incurred over 100 hours, the stress level must not exceed

$$S_2 = S_1/3.17 = 1000 \text{ psi}/3.17 = 315 \text{ psi}.$$

For $n = 8$, then $\sqrt[8]{100} = 1.78$ and

$$S_2 = 1000/1.78 = 562 \text{ psi}.$$

Thus, it would seem that, as a generality, the maximum stress level should be maintained at 500 psi or less. It will now be necessary to examine the individual stress components.

Gas Pressurization

The dimensional specifications call for an external diameter of 1/4 inch and an internal diameter of 1/8 inch. The external pressurization is to be 600 psi, and the internal pressurization is a function of the operating temperature and the working medium. As indicated in the earlier report, bismuth is a likely candidate for the working medium. At an operating temperature of 5000 R, the vapor pressure of bismuth is 531 psi.

By the theory for thick-wall cylinders, the tangential stress is

$$S_t = \frac{r_i^2 p_i - r_e^2 p_o}{r_e^2 - r_i^2} + \frac{(p_i - p_o) r_e^2 r_i^2}{r^2 (r_e^2 - r_i^2)}$$

where

S_t = circumferential stress, psi

p_i = internal pressure, psi

p_o = external pressure, psi

r_i = internal radius, in.

r_e = external radius, in.

For the case where the external-pressure value exceeds the internal-pressure value, as will be the case with bismuth, this tangential stress will be a compressive stress. It will have its maximum value at the internal wall, where $r = r_1$, since the second term varies inversely as the square of the radial position. For this maximum value at the inner wall, the expression for the circumferential stress becomes:

$$S_t = \frac{p_i (r_e^2 + r_i^2) - 2p_o r_e^2}{r_e^2 - r_i^2}$$

Then

$$S_t = \frac{2615 - 4800}{3} \text{ psi} = -728 \text{ psi.}$$

Again, by the theory for thick-wall cylinders, the radial stress is

$$S_r = \frac{r_i^2 p_i - r_e^2 p_o}{r_e^2 - r_i^2} - \frac{(p_i - p_o) r_e^2 r_i^2}{r^2 (r_e^2 - r_i^2)}$$

where

S_r = radial stress, psi

r = general radial position, in.

Other symbols are as previously defined.

Since this stress will be compared to or combined with the tangential stress, it will first be examined at the inner wall, where $r = r_i$; at this surface the radial stress is the negative of the gas pressure or

$$S_r = -513 \text{ psi.}$$

Combining these two stresses gives a shear stress

$$S_{s2} = \left| -728 + 513 \right| = 215 \text{ psi.}$$

This stress is within the stress range required for acceptable creep performance.

The next step will be to ascertain the axial stress and combine it with these tangential and radial stress values. The axial stress arises from two sources. The first source is the plug thrust coming from external pressurization on the end of the tube counterbalanced to some degree by the internal pressurization on the end of the bore. The second source is the bending moment associated with the deflection of the tube by the flowing gas stream. The plug stress will be a constant, but the bending stress will vary along the length of the tube. The plug stress can be determined by a force balance in the axial direction:

$$-\pi r_e^2 p_o = \pi [\, r_e^2 - r_i^2\,] S_p - \pi r_i^2 p_i$$

$$S_p = -\frac{r_e^2 p_o - r_i^2 p_i}{r_e^2 - r_i^2} \quad .$$

Again, making a numerical insertion gives

$$S_p = \frac{-1887}{3} \text{ psi} = -629 \text{ psi.}$$

Aerodynamic Loading

To calculate the bending moment it was necessary to specify the type of loading imposed upon the cantilever mounted tube. The loading (thrust) specified here was an aerodynamic loading:

$$\text{Th} = C_D A \frac{1}{2} \rho V^2 \,,$$

where

Th = thrust, lb

C_D = aerodynamic drag coefficient, dimensionless

A = area presented by specimen to the gas stream, ft^2

ρ = gas density, $slugs/ft^3$

V = gas stream velocity, ft/sec

For a Reynold's number, calculated to be about 13,000, the drag coefficient has a value C_D = 1.1. Then the loading can be expressed as

$$Th = \frac{1.1}{2} A\rho V^2 = 0.55 A\rho V^2 \ .$$

For dimensional consistency, the units of area must be square feet, with the velocity in feet per second. It is more instructive to put the area in terms of square inches and express it as a product of linear dimensions. The tube presents to the gas stream a projected area equal to the external diameter multiplied by the length. Making these substitutions gives

$$Th = \frac{0.55}{144} L \ (in.) \ d_e \ (in.) \ \rho V^2 \ lb \ .$$

This may then be reexpressed as a uniform load per unit length,

$$\frac{Th}{L} = th = 0.382 \times 10^{-2} d_e \rho V^2 \ lb/in. \ ,$$

which is suitable for calculation of the bending moment.

The aerodynamic loading (Figure A-32) was thus calculated to be 1/2 pound per linear inch. The length of the probe is specific as 1-1/2 in., so the aerodynamic load is a distributed load of about 3/4 pound.
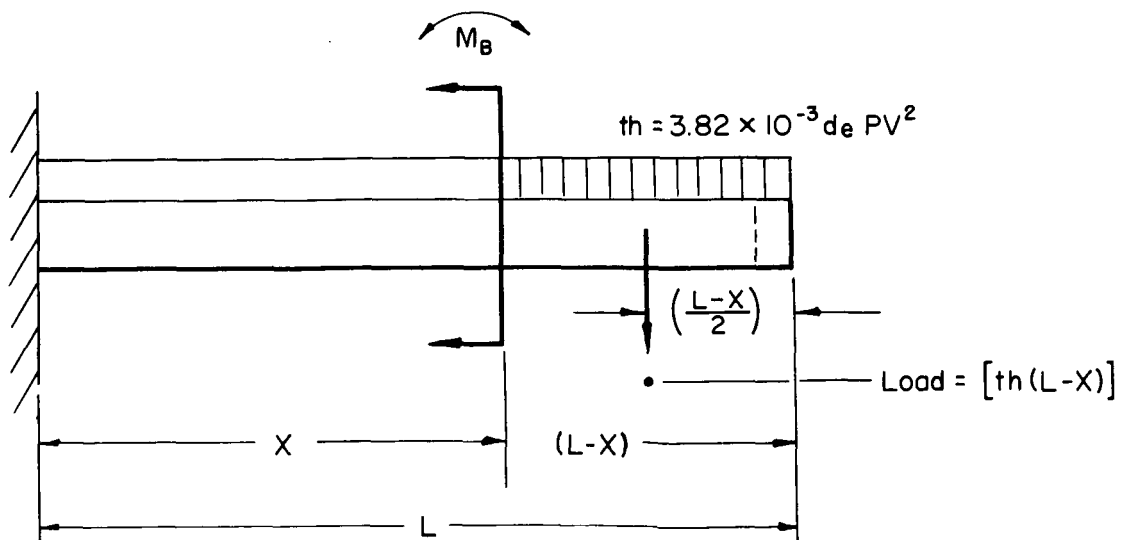

FIGURE A-32. AERODYNAMIC LOADING

A-49322

The convention previously adopted in these quarterly reports has been to measure axial distance from the cold wall; this convention is followed here in Figure 5.

The maximum value of the circumferential stress occurs at the inner wall. To complete the analysis, it was necessary to compute the bending stress:

$$S_B = \frac{M_B}{I/C} = \frac{0.191 \times 10^{-2} \, d_e \, \rho V^2}{I/C} (L-X)^2 \text{ psi.}$$

For the inner wall,

$$S_B = \frac{79.8 \, \rho V^2}{480} (L-X)^2 \text{ psi} = \frac{\rho V^2}{6.02} (L-X)^2 \text{ psi} \quad .$$

Using $\rho = 6.98 \times 10^{-4}$ slug/ft^3 and $V = 800$ ft/sec, the expression for S_B becomes

$$S_B = \frac{6.98 \times 64}{6.02} (L-X)^2 \text{ psi} = 74.2 \, (L-X)^2 \text{ psi.}$$

These calculations show that the maximum axial stress due to bending and plug force at the inner tube surface is a compressive stress of 796 psi on the downstream side and a minimum of 462 psi on the upstream side, both at the base of the probe.

Shear Stresses

Combining these with the tangential and radial stresses from pressurization, the shear stresses applicable to the maximum shear criteria are

$$S_{s1} = \left| S_a - S_t \right| = \left| -796 + 720 \right| = 68 \text{ psi}$$

$$S_{s3} = \left| S_r - S_a \right| = \left| -513 + 796 \right| = 283 \text{ psi.}$$

Accordingly, these stresses fall within the acceptable range for satisfactory creep performance.

At the outer wall, the circumferential stress has the value

$$S_t = \frac{-19'74}{3} = -658 \text{ psi} \quad .$$

The radial stress is the negative of the gas pressure,

$$S_r = -600 \text{ psi} \quad . \quad .$$

By similar analysis, the pertinent stress levels for the maximum shear criteria are

$$S_{s1} = \left| S_a - S_t \right| = \left| -963 + 658 \right| = 305$$

$$S_{s2} = \left| S_t - S_r \right| = \left| -658 + 600 \right| = 58$$

$$S_{s3} = \left| S_r - S_a \right| = \left| -600 + 963 \right| = 363 \quad .$$

Again, these stresses are within the allowable range for tungsten at 5000 R for satisfactory creep performance, particularly since they occur at the probe base where temperatures will be appreciably lower than 5000 R.

By the analysis above, it must be concluded that creep will not be a serious problem. The configuration gives all compressive stresses for a nonvibrating probe and they are compensating when inserted into the maximum-shear-theory criteria. The extrapolation of the stresses computed by maximum shear theory to estimates of creep is a tentative step; however, in the absence of a mark precise creep theory, it is justifiable.

Thermal Analysis

Nomenclature

The following nomenclature was employed in the text of the thermal-analysis section and will be employed throughout this Appendix.

T – temperature

t – time

h – convective coefficient

ρ – density of probe material

C_p – specific heat of probe material

L – volume/surface area ratio for probe

τ – a nondimensional parameter, $t(h/\rho C_p L)$

σ – the Stefan-Boltzmann constant

ϵ – emissivity of probe material

T_f – hot-gas temperature (absolute units)

A – a nondimensional parameter, $h/\epsilon T_f^3$

q – internal volumetric heat generation rate

G – a nondimensional parameter, qL/hT_f

ν – temperature ratio, T/T_f

ν_s – steady-state value of ν

T_s – steady-state value of T

T_c – temperature of cold walls which probe radiates to

$$\nu_c - T_c/T_f$$

a,b,c,d — constants

Z — coefficient of ν in the factor, $\nu^2 + Z\nu + R$, of $\nu^4 + A\nu - B = 0$

R — the factor in $\nu^2 + Z\nu + R$

x,y — real roots of $\nu^4 + A\nu - B = 0$

k — thermal conductivity

r — radial direction

z — axial direction

Response

If one considers a heat balance on a mass of material of very high thermal conductivity including convective interchange with a sink of T_f, radiative interchange with a sink of T_c, and a volumetric internal-heat-generation rate of q, the following differential equation results:

$$\frac{dT}{dt} = \frac{-h}{L\rho C_p}(T-T_f) - \frac{\sigma\epsilon}{L\rho C_p}(T^4 - T_c^4) + \frac{q}{\rho C_p} \quad . \tag{A-1}$$

Equation (A-1) can be generalized and made nondimensional by the following transformations:

$$\nu = T/T_f \tag{A-2}$$

$$\tau = t(h/\rho C_p L) \quad . \tag{A-3}$$

Under these transformations, Equation (A-1) becomes

$$\frac{d\nu}{d\tau} = -\frac{\sigma\epsilon T_f^3}{h}\nu^4 - \nu + \frac{qL}{hT_f} + \frac{q\epsilon T_f^3 \nu_c^4}{h} + 1 \tag{A-4}$$

or to integrate:

$$\int_{\nu_o}^{\nu} \frac{d\nu}{\nu^4 + A\nu - B} = -\frac{1}{A}\int_o^{\tau} d\tau \tag{A-5}$$

where

$$A = h/\sigma\epsilon T_f^3 \tag{A-6}$$

and

$$B = (qL/hT_f + 1)A + \nu_c^4 \quad , \tag{A-7}$$

or

$$B = (G + 1) A + \nu_c^4 \quad . \tag{A-8}$$

Thus, ν as a function of τ is dependent only on τ, A, and B.

To integrate Equation (A-5), one must assume A and B to be constant. However, ν_c is not constant, but at any time $\nu_c^4 <<< \nu^4$ so that for the particular application, ν_c is taken to be zero.

Equation (A-5) may be factored to facilitate integration.

$$\int_{\nu_0}^{\nu} \left(\frac{a\nu + b}{\nu^2 + Z\nu + R} \right) d\nu + \int_{\nu_0}^{\nu} \frac{c}{\nu - x} d\nu + \int_{\nu_0}^{\nu} \frac{d}{\nu - y} d\nu = -\frac{1}{A} \int_0^{\tau} d\tau \quad . \tag{A-9}$$

a,b,c, and d can be determined by equating coefficients. x and y are the real roots of $\nu^4 + A\nu - B = 0$. ν_0 is taken as zero for the integration. If other than an initial cold condition is desired, the time required is obtained by subtracting the time for ν to go from zero to ν_0 from the time for ν to go from zero to ν. The integration of Equation (A-9) under this condition yields

$$-\frac{\tau}{A} = \frac{a}{2} \ln \left[\frac{\nu^2}{R} + \frac{Z}{R} \nu + 1 \right] +$$

$$\left(\frac{2b - aZ}{\sqrt{4R - Z^2}} \right) \left\{ \tan^{-1} \left[\frac{2\nu + Z}{\sqrt{4R - Z^2}} \right] - \tan^{-1} \left[\frac{Z}{\sqrt{4R - Z^2}} \right] \right\} \tag{A-10}$$

$$+ c \ln \left(1 - \frac{\nu}{x} \right) + d \ln \left(1 - \frac{\nu}{y} \right) \quad .$$

Various values of ν are taken and the required values of τ to reach the corresponding value of ν is computed. Figures 10, 11, and 12 in the text resulted from Equation (A-10).

Steady State

The steady-state solution is obtained by setting $d\nu/d\tau$ in Equation (A-4) equal to zero, yielding:

$$1 - \frac{\sigma \epsilon T_f^3}{h} \nu^4 - \nu + \frac{qL}{hT_f} + \frac{\sigma \epsilon T_f^3 \nu_c^4}{h} = 0 \tag{A-11}$$

or

$$-\nu^4 - A\nu + B = 0 \quad . \tag{A-12}$$

The real roots (x and y) of Equation (A-12) were determined by a numerical technique. The positive root corresponds to the steady-state temperature while the negative root has no physical significance.   These results are shown as Figure 13 in the text.

DISTRIBUTION LIST

NASA-Lewis Research Center
21000 Brookpark Road
Cleveland, Ohio 44135
Attention Miles O. Dustin (10)

NASA-Lewis Research Center
21000 Brookpark Road
Cleveland, Ohio 44135
Attention Norman T. Musial (1)

NASA-Lewis Research Center
21000 Brookpark Road
Cleveland, Ohio 44135
Attention Adolph Lovoff
SNPO (2)

NASA-Lewis Research Center
21000 Brookpark Road
Cleveland, Ohio 44135
Attention Office of Reliability and
Quality Assurance (3)

NASA-Flight Research Center
P. O. Box 273
Edwards, California 93523
Attention Library (1)

Jet Propulstion Laboratory
4800 Oak Grove Drive
Pasadena, California 91103
Attention Library (1)

NASA-Manned Spacecraft Center
Houston, Texas 77001
Attention Library (1)

NASA-Western Operations
150 Price Boulevard
Santa Monica, California 90406
Attention Library (1)

Aerojet General Corporation
Sacramento, California
Attention T. F. McGrath (1)

Advanced Technology Laboratories
369 Whisman Road
Mountain View, California
Attention John Chambers (1)

NASA-Lewis Research Center
21000 Brookpark Road
Cleveland, Ohio 44135
Attention John J. Fackler
AD&E Procurement Sec. (1)

NASA-Lewis Research Center
21000 Brookpark Road
Cleveland, Ohio 44135
Attention Library (5)

National Aeronautics and Space
Administration
Washington, D. C. 20546
Attention NPO/F. C. Schwenk (3)

NASA-Ames Research Center
Moffett Field, California 94035
Attention Library (1)

NASA-Goddard Space Flight Center
Greenbelt, Maryland 20771
Attention Library (1)

NASA-Langley Research Center
Langley Station
Hampton, Virginia 23365
Attention Library (1)

NASA-Marshall Space Flight Center
Huntsville, Alabama 35812
Attention Library (1)

Westinghouse Astronuclear
Laboratory
Large, Pennsylvania
Attention R. L. Ramp (1)

Parametrics Inc.
221 Crescent Street
Waltham 54, Massachusetts
Attention E. H. Carnevale (1)

Rocketdyne
6633 Canoga Avenue
Canoga Park, California
Attention John Perow (1)

Minneapolis Honeywell
2600 Ridgway Road
Minneapolis 40, Minnesota
Attention F. W. Kuether   (1)

Bell Aerosystems Company
P. O. Box 1
Buffalo 5, New York
Attention J. V. Robinson   (1)

Bendix Research Division
Southfield, Michigan
Attention D. J. Niehaus   (1)

Los Alamos Scientific Laboratory
Los Alamos, New Mexico
Attention Dr. Josephy Perry, Jr.
          Group N4   (1)

General Electric Company
Advanced Technology Services
Cincinnati 15, Ohio
Attention W. E. Niemuth   (1)

Rosemount Engineering Company
4900 West 78th Street
Minneapolis 24, Minnesota   (1)

Wright-Patterson Air Force Base
Dayton, Ohio
Attention Harry Snowball
          AFFDL (FDCL)   (1)

General Electric Company
5100 West 164th Street
Cleveland, Ohio 44135
Attention M. Toth   (1)

NASA Scientific and Technical
  Information Facility
Box 5700
Bethesda, Maryland
Attention NASA Representative   (6)

NASA-Lewis Research Center
21000 Brookpark Road
Cleveland, Ohio 44135
Attention Report Control Office   (1)

NASA-Lewis Research Center
21000 Brookpark Road
Cleveland, Ohio 44135
Attention Nuclear Rocket
              Technology Office   (1)

NASA-Lewis Research Center
21000 Brookpark Road
Cleveland, Ohio 44135
Attention Dr. John C. Liwosz   (1)

U. S. Atomic Energy Commission
Technical Reports Library
Washington, D. C.   (3)

U. S. Atomic Energy Commission
Technical Information Service
  Extension
P. O. Box 62
Oak Ridge, Tennessee   (3)

Aerojet-General Corporation
Building 2019A2
Department 7411
Sacramento, California
Attention Dr. K. Sato   (1)

NASA Headquarters
Washington, D. C. 20546
Attention John E. Morrissey   (1)